

# The *Chandra* Observation of the Shell of Nova Persei 1901 (GK Persei): Detection of localized Non-thermal X-ray Emission from a Miniature Supernova Remnant

Şölen Balman

*Middle East Technical University, İnönü Bulvarı, Ankara, Turkey, 06531;  
solen@astroa.physics.metu.edu.tr*

## ABSTRACT

I present the data of the shell of classical Nova Persei (1901) obtained by the Advanced CCD Imaging Spectrometer S3 detector on-board *Chandra* Observatory. The X-ray nebula is affected mostly by the complex interstellar medium around the nova and has not developed a regular shell. The X-ray nebula is lumpy and asymmetric with bulk of emission coming from the southwestern quadrant. The brightest X-ray emission is detected as an arc that covers from the west to the south of the central source. Part of this feature, which is co-spatial with the brightest non-thermal radio emission region, is found to be a source of non-thermal (synchrotron) X-ray emission with a power law photon index of  $2.3_{-0.9}^{+1.5}$  and  $\alpha=0.68_{-0.15}^{+0.03}$  at about a flux of  $1.7 \times 10^{-13}$  erg cm<sup>-2</sup> s<sup>-1</sup>. This confirms that the shell is a site of particle acceleration, mainly in the reverse shock zone. There are strong indications for nonlinear diffusive shock acceleration occurring in the forward shock/transition zone with an upper limit on the non-thermal X-ray flux of  $1.0 \times 10^{-14}$  erg cm<sup>-2</sup> s<sup>-1</sup>. The total X-ray spectrum of the nebula consists of two prominent components of emission (other than the resolved synchrotron X-ray emission). The component dominant below 2 keV is most likely a non-equilibrium ionization thermal plasma of  $kT_s=0.1-0.3$  keV with an X-ray flux of  $1.6 \times 10^{-11}$  erg cm<sup>-2</sup> s<sup>-1</sup>. There is also a higher temperature,  $kT_s=0.5-2.6$  keV, embedded,  $N_H=(4.0-22.0) \times 10^{22}$  cm<sup>-2</sup>, emission component prominent above 2 keV. The unabsorbed X-ray flux from this component is  $1.5 \times 10^{-10}$  erg cm<sup>-2</sup> s<sup>-1</sup>. The X-ray emitting plasma is of solar composition except for enhancement in the elemental abundances (mean abundances over the remnant) of Ne/Ne<sub>⊙</sub> and N/N<sub>⊙</sub> in a range 13-21 and 1-5, respectively. A distinct emission line of neon, He-like Ne IX, is detected which reveals a distribution of several emission knots/blobs and shows a cone-like structure with wings extending toward NW and SE at expansion velocities about 2600 km s<sup>-1</sup> in the X-ray wavelengths.

arXiv:astro-ph/0503131v1 7 Mar 2005

The emission measures yield an average electron density in a range 0.6-11.2  $\text{cm}^{-3}$  for both of the components (filling factor=1). The electron density increases to higher values  $\sim 300 \text{ cm}^{-3}$  if the filling factor is decreased substantially. The mass in the X-ray emitting nebula is  $(2.1-38.5)\times 10^{-4} M_{\odot}$ . The X-ray luminosity of the forward shock  $\sim 4.3\times 10^{32} \text{ erg s}^{-1}$  indicates that it is adiabatic. The shocked mass, the X-ray luminosity and comparisons with other wavelengths suggest that the remnant has started cooling and most likely is in a Sedov phase.

*Subject headings:* X-rays: stars — radiation mechanisms: thermal, non-thermal — supernova remnants — shock waves — binaries: close — novae, cataclysmic variables — stars: Individual (GK Persei)

## 1. INTRODUCTION

Nova Persei 1901 (GK Per) is one of the most extensively observed and studied classical nova shells over the entire electromagnetic spectrum. It is known to be a fast ONeMg nova with  $V_{eject} \simeq 1200 \text{ km s}^{-1}$ ,  $M_{eject} \simeq 7 \times 10^{-5} M_{\odot}$  and distance  $\simeq 470 \text{ pc}$  (Payne-Gaposchkin 1957; Mc Laughlin 1960, Pottasch 1959). Nova Persei (1901) is the first recorded nova to show a light echo due to the reflection of light off the nearby interstellar material (Kapteyn 1901). Coudrec (1939) shows that the light echo region and the reflection nebula detected later in 1917 (Barnard 1917; Oort 1951) around GK Per are results of large-scale circumstellar sheets of dust clouds.

The optical remnant is  $103\times 90 \text{ arcsec}^2$  (diameter  $\sim 0.23 \text{ pc}$ ). The images show high asymmetry and the remnant has evolved into series of knots and filaments. The bulk of emission arises in the southwestern quadrant indicating interaction between the nova ejecta and the ambient gas (Slavin, O'Brien & Dunlop 1995, Seaquist et al. 1989). Furthermore, the remnant is detected with the Very Large Array (VLA) at 1.49 & 4.86 GHz as a non-thermal, polarized radio source with a spectral index of -0.67 and a flux of 24 mJy at 1 GHz (Reynolds & Chevalier 1984). In addition, the flux densities are 8.7, 20.6, 29, 33 and 38 mJy at frequencies 4.86, 1.49, 0.608, 0.408 and 0.327 GHz, respectively (Biermann, Strom, & Falcke 1995). This shows the existence of shocked circumstellar or interstellar material. The Infrared Astronomical Satellite (IRAS) observations at  $60\mu\text{m}$  and  $100\mu\text{m}$  reveal a symmetric far-IR emission region extending around the nova out to 6 pc ( $17'$  either side) suggested to be an ancient Planetary Nebulae associated with the binary (Bode et al. 1987; Bode, O'Brien, & Simpson 2004). Recent optical wavelength observations of the vicinity of GK Per show that some of this symmetric nebulosity is produced during the quiescent mass-loss phase of the central binary because of the evolved nature of the secondary (Tweedy 1995).

More recent IR observations also indicate that the IR emission within  $17'$  of the source is of material originating from the secondary (Dougherty et al. 1996). Scott, Rawlings, & Evans (1994) have discovered symmetric blobs of CO emission bracketing the central object at about  $\pm 200$  arc seconds. Overall, it is widely believed that the GK Per nebula behaves like a young Supernova Remnant (SNR) in the pre-Sedov phase interacting with its dense circumstellar medium.

Classical novae are a subset of cataclysmic variables which are interacting binary systems hosting a main-sequence secondary (sometimes a slightly evolved star) and a collapsed primary component, a white dwarf (Warner 1995). An outburst on the surface of the white dwarf as a result of a thermonuclear runaway in the accreted material causes the ejection of  $10^{-3}$  to  $10^{-7} M_{\odot}$  of material at velocities up to several thousand kilometers per second (Shara 1989; Livio 1994; Starrfield 2001). Though there has been no previous detection of old classical nova remnants in the X-ray wavelengths (evolving like Supernova remnants), classical nova remnants have been detected in the hard X-rays (above 1 keV) as a result of wind-wind interactions *in the outburst stage* (Balman et al. 1998; Mukai & Ishida 2001; Orio et al. 2001; Ness et al. 2003). In general, the hard X-ray radiation above 1 keV emitted from the hot shocked gas in nova remnants should be a powerful diagnostic for the nature of mass-loss mechanisms in classical nova outbursts together with the morphology, the elemental abundances and the evolution of nova shells. A long-sought insight into this issue has been gained with the discovery of the remnant old shell of classical nova Persei (1901) in the X-ray wavelengths.

The X-ray shell around GK Per was first discovered in a 50 ksec exposure with the ROSAT High Resolution Imager (HRI) (Balman & Ögelman 1999). The X-ray nebula extended to  $46''$  southwest,  $60''$  northwest,  $52''$  southeast, and  $43''$  northeast of the point source with an elliptical shape and lumpy morphology. The count rate of the shell was found as  $0.01 \pm 0.001$  c s $^{-1}$ . The estimated spectral parameters of the nova shell were:  $N_H \sim 1.3 \pm 0.3 \times 10^{21}$  cm $^{-2}$ , and  $kT \sim 0.16 \pm 0.03$  keV ( $\sim 2 \times 10^6$  K). The implied unabsorbed X-ray flux was  $F_x \sim 3.0 \times 10^{-12}$  erg cm $^{-2}$  s $^{-1}$  with  $L_x \sim 8.0 \times 10^{31}$  erg s $^{-1}$  (470 pc). In general, what was detected by the ROSAT HRI were the condensations in the shell. Since the ROSAT HRI did not have any adequate spectral resolution, a *Chandra* Advanced CCD Spectrometer (ACIS) observation was proposed.

In this paper, I present the characteristics of the *Chandra* spectrum, its components, and the detailed morphology of the shell. Finally, I discuss the results in comparison with the observations in the other wavelengths together with their implications on the novae theory and evolution of the classical nova shells.

## 2. THE OBSERVATION AND THE DATA

GK Per and its vicinity is observed using the *Chandra* (Weisskopf, O’deh, & van Speybroeck 1996) Advanced CCD Imaging Spectrometer (ACIS; Garmire et al. 2000) for a 95 ksec on 2000 February 10, pointed 1 arc minute offset from the nominal point on S3 (the back-illuminated CCD) with no gratings in use yielding a moderate non-dispersive energy resolution. The data are obtained at the FAINT mode. *Chandra* has two focal-plane cameras and two sets of transmission gratings that can be inserted in the optical path (HETG and LETG; High and Low Energy Transmission Gratings). The ACIS is used either to take high resolution images with moderate spectral resolution or is used as a read out device for the transmission gratings. ACIS is comprised of two CCD arrays, a 4-chip array, ACIS-I (four front-illuminated CCDs); and a 6-chip array, ACIS-S (four front-illuminated and two back-illuminated CCDs). The spectral resolution of ACIS arrays varies depending on the type of CCD in use, front or back illuminated CCDs, and the row numbers in the given CCD as a function of distance from the read out node or the aim point. The ACIS-S3 has a moderate spectral resolution  $E/\Delta E \sim 10-30$  (falls to about 7 below 1 keV) with an unprecedented angular resolution of  $0''.49$  per pixel (half-power diameter). The *Chandra* X-ray Center (CXC) has carried out the standard pipeline processing on the raw ACIS events, producing an aspect-corrected, bias-subtracted, graded (limited to grade 02346) and gain-calibrated event list (revision 2 data). In order to double check the standard processing, ”ACIS process events” thread is used to calibrate the level 1 data using the necessary gain and ”feff” files with the aid of CIAO 3.1 and the suitable CALDB (v.2.27-28). The data analysis is performed with CIAO version 2.1, 2.2 in the preliminary conference proceedings Balman (2002a,b) and in this paper with versions 2.3 and 3.1 along with XSPEC version 11.2.0/11.3.0 and XIMAGE version 4.0 for data preparation, spectral and spatial analysis. Prior to the analysis, the data are also filtered from the effects of the random flaring that occur during the observations with the ACIS-S by excluding events that are  $3\sigma$  above the mean count rate in the light curve which reduced the exposure time to about 81 ksec after cleaning. A preliminary analysis of the data could be found in Balman (2002a,b).

*Chandra* Observatory provides good spatial resolution data with high sensitivity thus, an 81 ksec observation provides an excellent opportunity to detect faint X-ray sources in the given region of the sky. To utilize this, the CELLDETECT algorithm (Harnden et al. 1984) is used to detect sources in the whole *Chandra* field image. As a result, 16 new X-ray sources are detected over  $6\sigma$  confidence level above the background (Küpcü-Yoldaş & Balman 2002). Most of the sources are found as possible Extragalactic sources. Some of them could also be a Galactic Cataclysmic Variable, a Low-mass X-ray Binary or a cooling Neutron Star.

### 3. THE CHANDRA IMAGE OF THE X-RAY NEBULA

The bright X-ray nebula extends to 52" South, 41" North, 45" West, and 38" East of the point source with an irregular shape, most counts coming from a region centered at the SW. The count rate from the vicinity of the shell is  $0.10 \pm 0.01 \text{ c s}^{-1}$ . The count rate ratio of the hemisphere centered around NE to the one centered on the SW is 2:3. Figure 1 displays an exposure corrected image of the nebula between 0.3 and 10 keV obtained with the *Chandra* ACIS-S (S3). The ACIS transfer streak is cleaned and the pileup PSF of the central source is removed from the raw image. The central source (the binary system) is extracted by modeling a two-dimensional PSF normalized to  $1.65 \text{ c s}^{-1}$  (i.e., similar to the source count rate without pileup) using ChaRT and MARX (version 4.08) (see also section 4.1 and 4.2). Figure 1 shows emission from the shell that is  $2\sigma$  above the background with a resolution of  $0''.5$  per pixel. A variable smoothing is applied on the image using a Gaussian of  $\sigma=0''.5-1''$ . The shell is not well developed with an average surface brightness of  $(4.9 \pm 2.9) \times 10^{-9} \text{ photons cm}^{-2} \text{ s}^{-1} \text{ arsec}^{-2}$ . The X-ray nebula shows complex lumped morphology with structure (eg., clump/blob/filament) sizes constrained by the smoothing performed on the image  $\sim 1''-2''$ . Large scale features could be collections of smaller clumps/blobs or arcs and filaments which indicate radial elongations. It has a central circular region brighter on the western side and there is a rather faint conical emission region more extended compared with the central brighter part (see section 6).

### 4. ANALYSIS ON THE CHANDRA SPECTRUM OF THE NOVA REMNANT

Since the *Chandra* observation was the first detection of the spectrum of such a nebula around a classical nova, several different models were tested on the data to understand the characteristics. The search showed that no single model could be fitted to the spectrum of the entire shell with a  $\chi^2_\nu$  better than 8. The spectrum of the entire nova shell showed a thermal plasma emission below 2 keV. The harder X-ray tail of the spectrum above 2 keV was also best fitted with a thermal plasma emission model. Equilibrium or non-equilibrium ionization models yielded similar fits. A power law model was ruled out for the spectrum of the entire remnant because of the non-physical spectral indices derived from the results in contrast with the non-thermal (synchrotron emission) nature of the radio data (Balman 2002a). The spectrum was remarkably flat above 2 keV. Figure 2 shows the best fitted two-component emission model of VMEKAL (Mewe, Gronenschild & van den Oord 1985; Liedahl et al. 1995) + PSHOCK (Borkowski et al. 1996). The shell photons were extracted using an annulus with an inner radius of  $12''.5$  and an outer radius of  $67''.5$ . The background was

also derived from an annular region farther out around the nova normalized to the source extraction region. The spectrum was calculated using a minimum of 50 counts per bin and the channels below 0.3 keV and above 9 keV were excluded due to low statistics.

The spectral parameters that were derived from the fits to the second component resulted in a very high shock temperature in excess of 50 keV and shock speed larger than  $5000 \text{ km s}^{-1}$  which were inconsistent with all the measurements in the other wavelengths. This problem was largely due to the excess photon contribution from the wings of the PSF of the piled-up central source. Such a contaminating component resulted in significantly higher temperature and flux for the second component above 2 keV, and shifts in the central line energies (toward lower energies) of the lower temperature component below 2 keV. This excess emission compared with the observed PSF of the central source also needed to be properly cleaned in order to study the image of the shell. Sections (4.2) and (4.3) describe the problem and the procedure/method used to clean and remove this effect of the PSF wings from the shell data (i.e, images and spectra).

#### 4.1. The Contamination of the Shell Image by the Central Source

Pileup results in the CCDs when two or more photons are detected as a single event. The consequences are spectral hardening since apparent energy is approximately the sum of two (or more) energies and underestimation of the true counting rate of the point sources. It is expected that pileup problem also distorts the PSF of the central source by creating holes at the centers (pulse saturation) and the PSF wings become more prominent as the count rates increase. As a result, appreciable central source counts can be detected in a region within  $2'$  of the pointed source. This contaminates any extended emission in the close vicinity of the central source. The source photons of GK Per has a pileup of about 89% where one expects the emission from the shell to be affected by the pileup PSF and the prominent PSF wings. In order to exclude the spectrum of the central source, GK Per, the nova shell photons are extracted from an annular region of  $12''.5$  to  $67''.5$  in radius (as presented in sec 4.0). This should largely avoid the contamination from the piled-up central source, but it will be inefficient to exclude the effects of the prominent PSF wings beyond  $12''.5$  out to  $67''.5$  in radius. To segregate the counts of the nova shell from the central source counts in the wings of the PSF (at the vicinity of the nova shell), an archival search within the ACIS-S pointings (no grating or HETG observations) has been performed. The prime motivation of the search has been to measure the count rate in the PSF wings in an annular region of  $12''.5$  out to  $67''.5$  radius in comparison with the count rate in a circular region of  $12''.5$  . The particular extraction radii is assumed only to compare the GK Per observation

with other archival observations. The two different regions assumed are designated as: (1) the *source* defined as the circular photon extraction region of  $12''.5$  radius (25 pixels), and (2) the *shell* defined as the annular photon extraction region of  $12''.5$  to  $67''.5$  in radius. The count rates within the *source* and *shell* regions are compared for several observations so that an acceptable estimate of the count rate in the wings of the PSF can be made for the central source of GK Per in the vicinity of the nova shell given the central source count rate of GK Per (pileup rate). Over 300 archival data of *pointed sources* on the ACIS-S array have been analyzed imposing several criteria : (1) energy spectrum of the source peaks about 1-2 keV and have a hard X-ray tail, (2) pointings are within a region of  $2'$  of the nominal point on ACIS S-3, (3) all observations have the same frame time of 3.2 sec and obtained in the Faint mode, (4) no special spatial filtering has been performed during the observation for pileup mitigation, (5) HETG observations with bright first order data have also been excluded, (6) observations with pileup count rates brighter than a few c/s (i.e. 3 c/s) are also excluded since the scaling relation is altered, (7) observations that show strong background flares and anomalous high background rates have been disregarded. As a result, about 15 suitable pointings have been recovered that fits all the criteria. Figure 3a shows the count rate in a region of  $12''.5$  radius (25 pixels), the *source*, versus the count rate in an annular region of  $12''.5$  to  $67''.5$  in radius, the *shell*, both centered at the point source. Finally, a scaling relation between the count rates in two different regions described as the *source* and *shell* is derived. The curve in Figure 3a is best fitted by the quadratic function,  $ax^2+bx+c$ , where  $a=-0.12\pm 0.09$ ,  $b=1.11\pm 0.14$ , and  $c=-0.18\pm 0.03$ . This has been used to approximate the count rate in the PSF wings of GK Per within the region covered by the classical nova shell. For a *source* count rate of  $0.2 \text{ c s}^{-1}$  (pileup rate), the estimated count rate in the PSF wings (*shell* region) within the classical nova shell is  $0.037 \text{ c s}^{-1}$ , which yields an actual nova shell count rate around  $0.063 \text{ c s}^{-1}$  (instead of  $0.1 \text{ c s}^{-1}$ ). This is also checked using an archival ACIS-S HETG data of GK Per obtained during a dwarf nova outburst. The zeroth order pileup source count rate is used to estimate the count rate in the described shell with the aid of the derived scaling relation (same extraction radii is assumed). Considering that a lower frame time, and spatial clipping are used to mitigate the pileup to some extent and that the source is in outburst, the scaling function yields similar results. I would like to note that the contamination problem described here could be important for *Chandra* ACIS observations of other astrophysical objects like Galaxies/Clusters and centrally filled composite SNRs.

In order to remove the central source from the image of the nova shell of GK Per together with the prominent PSF wings, a PSF is created using ChaRT. Several PSFs are merged to achieve the correct count rate within the nova shell region (i.e.,  $0.037 \text{ c s}^{-1}$  in the PSF wings). The final central source count rate of the combined PSF in the *source* region is close to the count rate (within 8%) of the central source, GK Per, when there is no pileup (1.7-1.8

$\text{c s}^{-1}$ ). The un-piled central source rate is calculated using an archival ASCA data of GK Per (i.e., spectrum) and PIMMS. Next, the combined PSF is extracted from the total image to achieve Figure 1.

## 4.2. The Cleaned Shell Spectra

The central source, GK Per, has 89% pileup and has about  $0.037 \text{ c s}^{-1}$  in the region of the X-ray shell due to its prominent PSF wings. Thus, this will also affect the "entire nova shell spectrum" where the spectrum of the central source will be appearing as a component of the nova shell spectrum of GK Per as a result of the counts in the PSF wings. I would like to note that though GK Per has a dusty environment, previous X-ray observations with several different satellites have not recovered any dust scattering halo around the source which could have affected the emission below 1 keV. The result of the analysis presented in section (4.1), for the sources which suffer from the pileup effect on ACIS-S3, indicates that the spectra derived from the *shell* regions (as denoted in section [4.1]), basically from the PSF wings, may be better approximated with the spectra derived from the *source* regions, but scaled down. This is only because the spectral shapes resemble each other, and not that the spectra from the PSF wings have pileup photons (as in the *source* regions). Theoretically, pileup in the PSF wings should either be non-existent or very small, however the spectra from the PSF wings may show spectral hardening. Figure 3b shows a collection of spectra of the sources used for calibration where the above assumptions can be clearly investigated. The upper curves represent the *source*-region spectra and the lower curves represent the *shell*-region spectra (spectra obtained from the PSF wings). The sources have very similar pileup source count rates to GK Per in the stated *source* extraction region  $0.19\text{-}0.21 \text{ c s}^{-1}$  (more or less similar central source spectra with a hard X-ray tail - three objects are other CVs). In order to remove the spectrum of the PSF wings of the central source from the nova shell spectrum, first a spectrum (of GK Per) is extracted from a circular region of radius  $12''.5$  (*source*-region). This spectrum is fitted with a composite model of photoelectric absorption, bremsstrahlung and power law models. The best fit parameters are used to recalculate/rescale this spectrum using both MARX and WEBSPEC yielding a count rate of  $0.037 \text{ c s}^{-1}$ . The parameters used to model this *source*-region spectrum are an  $N_H$  of  $1.16 \times 10^{22}$ , a covering fraction of 0.95, a kT of 13.3 keV, a bremsstrahlung normalization of  $5.54 \times 10^{-4}$ , a photon index of 2.5 and a power law normalization of  $7.93 \times 10^{-7}$ . Figure 4 shows the central source spectrum of GK Per derived from the *source*-region (upper curve), the modeled spectrum to be subtracted (middle curve), and the un-piled central source spectrum of GK Per (lower curve). The un-piled source spectrum is extracted from the out-of-time events of the ACIS transfer streak. I want to point out that all three data sets in Figure 4 are consistent with one another



and the un-piled source spectrum can be approximated with the modeled spectrum to an acceptable extend. Finally, the modeled spectrum (middle curve) is subtracted PI channel by PI channel from the nova shell spectrum of GK Per. Figure 5a shows the resulting total nova shell spectrum after removing the spectrum of the PSF wings of the central source, GK Per. The total number of nova shell photons between 0.3-1.6 keV is 4675 and between 1.6-8.0 keV is 410 after removal of the background and the photons from the wings of the central source PSF. The shell photons are extracted using an annulus with an inner radius of 12".5 and outer radius of 67".5 and regrouped using a signal-to-noise ratio of 13 per energy bin. The cleaned nova shell spectrum can not be fitted with a single emission component with reduced  $\chi^2_\nu$  of 4.0 (see Figure 5a). *There is excess emission above 1.6 keV that causes up to  $4\sigma$  deviations in the residuals when the data are fitted with a single spectral model.* In the rest of the paper, only analyses and results derived from the cleaned spectra/image will be presented, since there are significant differences between the cleaned and uncleaned data.

### 4.3. The First Component (below 2 keV)

The X-ray emission below 2 keV is found to be consistent with only the thermal plasma emission models. Figure 5b shows the data and the best fitted two-component emission model of VPSHOCK+NEI (Borkowski et al. 1996; Hamilton et al. 1983). The shell photons are extracted using an annulus with an inner radius of 12".5 and outer radius of 67".5. The background is also derived from an annular region farther out around the nova normalized to the source extraction region. The spectrum is calculated using a minimum of 50 counts per energy bin (or a Signal-to-noise ratio of 13 per energy bin, which made no difference in derived parameters). The PI channels below 0.3 keV and above 8 keV are excluded due to low statistical quality. The spectral parameters of the nova shell are an  $N_H$  of  $(0.1-3.7)\times 10^{21}$  cm<sup>-2</sup>, kT of 0.1-0.3 keV ( $\sim(3-4)\times 10^6$  K) and an emission measure (EM) in a range  $(0.2-54.5)\times 10^{54}$  cm<sup>-3</sup>. The noted error ranges correspond to  $2\sigma$  confidence level. The spectral parameters derived for this component using three different composite spectra are, also, displayed on Table 1. The unabsorbed soft X-ray flux is  $F_x \sim (0.03-11.8)\times 10^{-11}$  erg cm<sup>-2</sup> s<sup>-1</sup> yielding an X-ray luminosity of  $L_x \sim 4.3^{+26.1}_{-4.2}\times 10^{32}$  erg s<sup>-1</sup>. Any two-temperature ( $T_i \neq T_e$ ) non-equilibrium ionization plasma model yields similar  $T_i$  and  $T_e$  within  $2\sigma$  error ranges when fitted to the data below 2 keV.

The detected emission measure  $EM = \langle n_e \rangle^2 V_{eff}$  (after cleaning the shell spectrum) yields an average electron density  $n_e$  in a range 0.6-11.2 cm<sup>-3</sup> using a volume of  $4.3\times 10^{53}$  cm<sup>3</sup> (consistent with the X-ray photon extraction region) and a filling factor of 1 (i.e.,  $V_{eff}$  can be theoretically expressed as  $V_{eff} = 1.33\pi v^3 t^3 f$ ;  $v$  is the expansion velocity [see sec (1)],  $t$

is the elapsed time since the eruption, and  $f$  is the volume filling factor). If the filling factor is as low as  $1 \times 10^{-5}$ , then the electron density can be as high as  $84\text{-}712 \text{ cm}^{-3}$  ( $\sim 300 \text{ cm}^{-3}$ ). The time scale for equipartition between electrons and ions is

$$t_{e-i} \simeq 2.5 \times 10^6 \left( \frac{T_e}{10^9 K} \right)^{1.5} \left( \frac{n_e}{10^8 \text{ cm}^{-3}} \right)^{-1} \quad (1)$$

(Spitzer 1978; Fransson, Lundqvist & Chevalier 1996, hereafter FLC96). The derived range of the X-ray temperature ( $T_e \sim T_{shock}$ ) and the age of the remnant implies that the emitting plasma is in (for  $n_e \geq 60 \text{ cm}^{-3}$ ) or close to equilibrium. The ionization timescale ( $\tau = n_0 t$ ) of  $\tau < 1.7 \times 10^{11}$  detected using the PSHOCK (non-equilibrium ionization plasma) model indicates it is close to equilibrium with ambient density  $n_0 \leq 60 \text{ cm}^{-3}$  ( $t = 99$  years). This is supported by the HI measurements in the vicinity of GK Per where the column density infers an ambient density of  $20\text{-}30 \text{ cm}^{-3}$  (Seaquist et. al. 1989). The filling factor in the region where the first component arises is  $f > 0.0022$  calculated using  $n_0$  (thus,  $n_e = 4n_0$ ) and the range of EM derived from the spectral fits.

The third composite model on Table 1 (i.e., §3) is constructed to derive the detected line energies, line sigmas and fluxes together with the continuum temperature. The X-ray emitting plasma has mostly solar composition except for neon and nitrogen. The  $\text{Ne}/\text{Ne}_\odot$  is in a range 13-21 and  $\text{N}/\text{N}_\odot$  is in a range 1-5 (ratio of relative number fraction to H). The neon over-abundance is detected in a prominent emission line at around  $E_0 = 0.900\text{-}0.916 \text{ keV}$  ( $2\sigma$  range) corresponding to the position of the He-like Ne IX emission line triplet with a flux  $F = (1.7\text{-}11.0) \times 10^{-14} \text{ erg cm}^{-2} \text{ s}^{-1}$  (three separate lines are not resolved). The range of the central line energy support that the (He-like) Ne IX forbidden line emission may be more pronounced and that the first X-ray component is an under-ionized plasma, a non-equilibrium ionization plasma, cooling toward collisional equilibrium (the nonexistence of the H-like neon line will strengthen this). At around  $3\text{-}4 \times 10^6 \text{ K}$ , the neon is expected to start recombining. Nitrogen over-abundance is highly likely resulting from the He-like N VI emission line at  $E_0 = 0.412\text{-}0.433 \text{ keV}$  ( $2\sigma$  range) with a flux  $F = (0.35\text{-}3.16) \times 10^{-13} \text{ erg cm}^{-2} \text{ s}^{-1}$ . The spectral resolution of ACIS degrades at such energies and the line profile is smeared. The exclusion of the line causes deviation above three sigma level at around the line energy (Balman 2001). The shift in the central line energy toward lower energies is also observed for the N VI indicating a more prominent forbidden line emission.

The continuum temperature derived from the thermal bremsstrahlung fit to the data below  $2 \text{ keV}$  is consistent with the fits performed using the other models within errors. The two different Gaussians used to fit the data, yield the Ne and N lines as mentioned above. The third Gaussian has a central energy  $E_0 = 0.549\text{-}0.562 \text{ keV}$  ( $2\sigma$  range) which corresponds to the O VII emission line. This indicates that the low temperature plasma is also rich

in oxygen. A fit to the data with increased oxygen abundance yields an abundance 1-3 times the solar abundance of oxygen (ratio of relative number fraction to H). However, I need to caution that the O VII line overlaps with the maximum observed energy of emission of the low temperature component. An observation with the LETG/HETG (i.e., grating observations to resolve separate lines) on board *Chandra* to resolve the emission lines would be unfeasible for the shell because it has a very low surface brightness and a more recent HETGS observation of the central source shows no sign of the shell.

#### 4.4. The Second Component

The second component is found to be consistent either with a thermal plasma emission or a bremsstrahlung emission in origin. The spectral parameters obtained from the fits with the PSHOCK model are an  $N_H$  of  $(4.0-22.0) \times 10^{22} \text{ cm}^{-2}$ , a shock temperature of  $kT=0.5-2.6$  keV (best fit  $\sim 0.9$  keV) and an emission measure of  $(1.5-160.2) \times 10^{54} \text{ cm}^{-3}$ . Table 2 displays the spectral parameters for the entire shell derived from the three different composite model fits to the X-ray data above 2 keV. The ranges correspond to  $2\sigma$  confidence level and the fits are carried out simultaneously with the first component. Figure 5b shows a fitted composite spectrum. A very intriguing outcome from the spectral fits is the detection of a cold shell between the two components that shows high absorption from the neutral material within this zone. To clarify this, a fit with a single  $N_H$  parameter is shown in Figure 5c (see also Table 2) where significant excess above 2 keV is observed with  $\chi^2_\nu$  values of about 2.4. Moreover, the derived plasma temperature (using thermal plasma models) from fits with a single absorption ( $N_H$ ) parameter is very large compared with expectations. Thus, single absorption for both components of emission in the shell spectrum is non-physical. Fits with a non-thermal power law or SRCUT model also show non-physical results with positive spectral/photon indices (see Table 2) for a single absorption parameter for the entire shell spectrum. The detailed discussion on this issue can be found in section [7.1]. The ionization timescale (i.e.,  $\tau=n_0t$ ) is found as  $\tau=0.9^{+41.0}_{-0.8} \times 10^{10} \text{ s cm}^{-3}$ . The plasma shows no resolved emission lines. On the other hand, the high neutral hydrogen column density absorbs the X-ray emission below 1.5 keV where most of the emission lines (e.g., Ne and N) would be found. The unabsorbed X-ray flux of the high temperature component is  $F_x (0.5-25.0) \times 10^{-11} \text{ erg cm}^{-2} \text{ s}^{-1}$  consistent with an X-ray luminosity of  $L_x=(6.6-0.2) \times 10^{33} \text{ erg s}^{-1}$  (at 470 pc). The reduced  $\chi^2$  values do not differentiate between equilibrium and non-equilibrium ionization plasma emission models. The emission measure implies a minimum average electron density of  $2.0 \text{ cm}^{-3}$  (maximum  $19.3 \text{ cm}^{-3}$ ) over the volume stated in section (4.3) with a filling factor  $f=1$ . If the filling factor is decreased to about  $1 \times 10^{-4}$ , the electron density increases to about  $200 \text{ cm}^{-3}$ . The ionization timescale translates to ambient densities of  $n_0 < 130.6$

$\text{cm}^{-3}$  for the second component with  $4.1 \text{ cm}^{-3}$  calculated from the best fit results of the ionization timescale. Using the EM parameter values and scaling the electron density from the maximum limit on the ambient density ( $4n_0=n_e$ ), the filling factor is  $f > 0.0002$ .

Non-thermal power law and SRCUT (Reynolds 1998; Reynolds & Keohane 1999) models have also been applied to the shell spectrum above 2 keV. The resulting spectral parameters are an  $N_H$  of  $(6.0\text{-}16.0)\times 10^{22} \text{ cm}^{-2}$  (using two different  $N_H$  parameter), a photon index  $\Gamma=5.9$ , a spectral index  $\alpha=0.32$  and an unabsorbed X-ray flux  $F_x \geq 8.0\times 10^{-13} \text{ ergs s}^{-1} \text{ cm}^{-2}$ . Table 2 shows the detailed results of the fits using these models. The photon index implies steeper power law spectra not in accordance with the findings on SNRs that indicate existence of particle acceleration in the X-ray and radio wavelengths (see section [5.0]). Such values are in a range  $\Gamma=2\text{-}4$  within errors (Rho et. al. 2002, Berezhko et al. 2003). The spectral index is also inconsistent with the findings on the shell of GK Per in the radio wavelengths (see the Introduction).

## 5. THE DETECTION OF LOCALIZED NON-THERMAL X-RAY EMISSION FROM THE NOVA REMNANT AND SPECTRAL VARIATIONS

Once the whole spectrum of the shell is determined, spectral variations on smaller scales are examined. The remnant is divided into four azimuthal quadrants around the central source from position angle  $\text{PA}=0^\circ$  to  $\text{PA}=360^\circ$  centered on NW, NE, SE, and SW. Figure 6a shows a graphical representation of the extraction regions. The resulting spectra are simultaneously fit with a model similar to the spectrum of the entire shell. The spectral parameters show slight variations in different quadrants, but the variations are within  $2\sigma$  confidence level errors in most cases. The four spectra have count rates in a range  $0.019\text{-}0.006 \text{ c s}^{-1}$  (the spectrum of the PSF wings of the central source is removed with a similar method as described in sections 4.1 and 4.2). There are variations in each spectra at different energies below 1 keV (see Figure 6b). These could be related to variations in the line intensities (variation in elemental abundances could also be possible). NE quadrant has the least line intensity between 0.3-1 keV (see the  $4\sigma$  variation between NE and SW at around the energies corresponding to the O VII emission line in Figure 6b). The asymmetric morphology of the X-ray nebula is the result of the distribution of material in the circumbinary medium of the nova and geometrical effects.

The search for spectral variations over the entire remnant shows that the spectrum of the nebula with two thermal components is generally consistent over the whole remnant. On the other hand, the radio synchrotron emission from the nova shell strongly suggests

that non-thermal emission associated with the accelerated electrons should be recovered. Such a component that is not prominent enough to be detected from the entire shell, then could be localized within the shell. Most of the efforts to derive spectral variation across the remnant suffered from the low surface brightness of the shell except for the highest intensity zone at the edge of the remnant which is an arc of emission covering from NW to S of the X-ray nebula. This is also co-spatial with the brightest radio synchrotron emission region at 1.4 GHz (see section [6.1]). The spectrum of the brightest X-ray emission region, *Peak Spectrum*, is extracted from the edge of the shell using a sector that subtends about  $70^\circ$  to the central source with a width of nine arc seconds (the region denoted as (2) in Figure 6a). Next, the Peak Spectrum is cleaned using a similar procedure described in section (4.1 & 4.2). In addition, the rescaled source spectrum is corrected further using the total number of central source photons within the extraction annulus of the entire nova shell spectrum ( $\sim 3000$  counts) and a radial distribution of  $r^{-2}$  (i.e.,  $N(r) \sim Ar^{-2}$  see *Chandra* calibration pages for further details). The simulated central source spectrum (as described in section 4.2) is subtracted PI channel by PI channel from the Peak Spectrum. The cleaned Peak Spectrum is regrouped with a minimum of 20 counts per energy bin. The uncleaned Peak Spectrum has a count rate of  $0.0099 \pm 0.00072$  which reduces to  $0.00925 \pm 0.00057$  after the cleaning process is completed. It is apparent that the cleaning process is not crucial and necessary for the bright X-ray emission region since this region is far away from the central source and small enough so that the contribution from the PSF wings of the central source is marginal (below the local background). The total number of photons between 0.3-1.6 keV is 670 and between 1.6-8.0 keV is 105 after the removal of the background and the photons resulting from the wings of the central source PSF. Because of the low statistical quality PI channels below 0.3 keV and above 8.0 keV have been excluded.

An investigation of the cleaned Peak Spectrum, performing fits to the data reveals that it has two components. Table 3 displays all the results from fits with several composite thermal and non-thermal emission models. Figure 7a shows the Peak Spectrum fitted with a single model of emission where the reduced  $\chi^2_\nu$  value is 3.4 and the excess in the band 1.6-8.0 keV is significant. Thus, existence of two components of emission is justified. The first component resembles to that of the first component of the entire shell with similar spectral parameters. The spectrum of the second component from the X-ray Peak region, this time, yields consistent fits with the SRCUT or power law emission models as opposed to a thermal plasma model which yields non-physical results. All the fits thermal plasma models result in temperatures in excess of 7 keV ( $2\sigma$  lowest limit and best fit result  $\sim 20$  keV) which is inconsistent with the expectations from this remnant. The fits also reveal absorption difference between the two components in question and the fits involving a single absorption parameter for the two components yield significant excess in the 1.6-8.0 keV

range with reduced  $\chi^2_\nu$  value of 3.0 . Figure 7b and Figure 7c display examples of the fitted Peak Spectrum that has a two-component model with two different  $N_H$  parameter, and a two-component model with a single  $N_H$  parameter for both components, respectively. The spectral parameters for the second component derived using a simple power law model are an  $N_H$  of  $4.9^{+5.1}_{-3.7} \times 10^{22} \text{ cm}^{-2}$ , a photon index of  $\Gamma=2.3^{+1.5}_{-0.9}$  and an unabsorbed X-ray flux of  $1.7^{+73.0}_{-1.4} \times 10^{-13} \text{ erg s}^{-1} \text{ cm}^{-2}$ . The errors correspond to  $2\sigma$  confidence level. The X-ray flux of this non-thermal component translates to an unabsorbed X-ray luminosity of about  $4.6 \times 10^{30} \text{ erg s}^{-1}$ . More appropriate models for synchrotron emission (from SNRs) involve exponentially cut-off power law distribution of electrons in a magnetic field (Reynolds 1998; Reynolds & Keohane 1999). This is largely because the synchrotron losses or escaping particles are expected to decrease the flux density at the X-ray energies falling below the extrapolated radio spectrum. The cleaned spectrum from the X-ray Peak region (region [2] in Figure 6a) is fitted with the SRCUT model for a more proper treatment. The resulting parameters are :  $N_H=5.0^{+5.5}_{-1.7} \times 10^{22} \text{ cm}^{-2}$ ;  $\alpha=0.68^{+0.03}_{-0.15}$ ; and  $\nu_{break}=1.2^{+2.3}_{-0.3} \times 10^{18} \text{ Hz}$ . I would like to make a note that since the photon extraction region for the Peak Spectrum is very small and farther away from the central source, the cleaning process have slightly changed (i.e., corrected) the best fit parameters leaving the error ranges similar/unaltered (for both SRCUT and the power law models). The normalization parameter, which is the radio energy flux at 1 GHz (in Jy), is fixed at the calculated value of 0.024 Jy (Reynolds & Chevalier 1984; Biermann et al. 1995). The energy flux and the unabsorbed X-ray luminosity is the same as the values calculated for the simple power law model. The fit successfully recovers the correct spectral index  $\alpha$ , for the radio spectrum ( $\alpha=0.67$ ; see Introduction). This is also consistent with the range of X-ray spectral photon index. *Thus, emission from the same electron population has been detected as the extension from the radio wavelengths.*

It is expected to detect gamma-ray emission as well as X-rays from the shell-like SNRs primarily due to bremsstrahlung of accelerated relativistic electrons off pre-shock material together with contribution from an Inverse Compton emission (off of Cosmic Microwave Background), the pion decay interactions, and the secondary p-p interactions (Berezhko & Völk 1997; Grassier et al. 1998; Stunner et al. 1997; Baring et al. 1999, Berezhko et al. 2003 and references therein). The critical frequency (also the break frequency in the above paragraph) for synchrotron emission from an electron of energy E is

$$\nu_{break} = 3.2 \left( \frac{B \sin \theta}{2 \times 10^{-4} G} \right) \left( \frac{E}{GeV} \right)^2 GHz \quad (2)$$

(Chevalier 1999). Using the cut-off (break) frequency derived from the SRCUT model fits, I estimate  $E_{max} \simeq 15\text{-}30 \text{ TeV}$  for the maximum energy of accelerated electrons radiating at  $(0.4\text{-}1) \times 10^{18} \text{ Hz}$  for the remnant of GK per ( $B=75\text{-}47 \mu\text{G}$ ; Seaquist et al. 1989).

A spectrum is extracted from the outer ridge (outer ridge: region denoted as (3) in Figure 6a) using a PIE extraction region with a width of nine arc seconds (the same size annulus-sector as the photon extraction region of the Peak Spectrum). A fit with the SRCUT model of emission yields an  $N_H=2.2_{-0.7}^{+1.8}\times 10^{22}$  cm<sup>-2</sup>,  $\alpha=0.76_{-0.02}^{+0.03}$  and  $\nu_{break}\geq 1.8\times 10^{18}$  Hz ( $\chi^2_\nu=1.17$  (37)). The unabsorbed X-ray flux from the outer ridge is  $4.1_{-2.2}^{+2.0}\times 10^{-14}$  erg s<sup>-1</sup> cm<sup>-2</sup>. The spectrum of the inner ridge (inner ridge: region denoted as (1) in Figure 6a) is extracted, using a similar photon extraction region as in the derivation of the Peak Spectrum and the outer ridge (with a width of nine arc seconds). A fit with the SRCUT model of emission yields an  $N_H=2.1_{-1.3}^{+3.5}\times 10^{22}$  cm<sup>-2</sup>,  $\alpha=0.58_{-0.07}^{+0.07}$  and  $\nu_{break}=3.1_{-2.1}^{+4.0}\times 10^{16}$  Hz ( $\chi^2_\nu=0.7$  (23)). The unabsorbed X-ray flux from the inner ridge is  $1.1_{-0.07}^{+5.2}\times 10^{-13}$  erg s<sup>-1</sup> cm<sup>-2</sup>. All the spectra are cleaned (for the wings of the PSF of the central source) using a similar procedure to the Peak Spectrum where the amount of cleaned PSF photons is largest for region (1) and lowest for region (3). The fits with the SRCUT model for the regions 1, 2 and 3 in Figure 6a yield spectral indices consistent with the radio observations of the remnant which are found to be in a range 0.55-0.95 (between 1.4-4.9 GHz; see Seaquist et al. 1989). The radio spectral index is variable over the remnant where it is steepest at the outer ridge and more flat in the interior regions. The normalization of the SRCUT model fits is fixed at the calculated value of 0.024 Jy at 1 GHz as mentioned earlier. Thus, it is clear that there are three components in the spectrum of the X-ray nebula of GK Per: A cool thermal component associated with the forward shock/transition zone that shows line emission; a deeply embedded hot thermal component without emission lines and a "localized" embedded non-thermal power law (i.e., Synchrotron) emission component coming from the region where the shell interacts with the circumbinary medium around the nova. An elaboration of this scenario is in section [7.1].

## 6. THE Ne IX EMISSION LINE IMAGE AND DETAILED IMAGING OF THE REMNANT

The nebula displays a different structure compared with the broad band *Chandra* image at the emission line energy detected around 0.907 keV. The Ne IX emission line image shows a symmetric cone-like shape centered at the SW direction (see Figure 8) and the flattening on the SW is more prominent. The image is prepared by extracting the energy channels (0.8-1.0 keV) forming the full width of the line at the continuum level and subtracting on pixel-to-pixel basis a suitable continuum image from the line image using PI channels corresponding to 1.12-1.4 keV. This continuum image, also, subtracts out any central source photons since it includes both the source and the shell continuum in the channel range. I need to note that some of the line emission and diffuse neon emission could have been lost in this process, but Figure 8 is a cleaned image. Both of the line and continuum images are regrouped by

two pixels and smoothed by a Gaussian of  $\sigma=2''$  before subtraction. The resolution of the final image (continuum subtracted) is  $1''$  per pixel and shows emission from the shell that is  $2\sigma$  above the background. The neon image of the shell clearly reveals a cone, a one sided shell (i.e., hemisphere), where the remnant rams into a wall like structure and is compressed in that direction. The image also shows a very lumpy morphology with clump sizes limited by the resolution of the image  $\sim 2''$ . The size of the cut-cone is  $\sim 63''$  in the flattened zone and  $\sim 112''$  - $116''$  in the wings toward the North and East in the image. Assuming 99 years for the elapsed time and a linear expansion law, the velocities required to create the wings are  $\sim 2600$ - $2800$  km s $^{-1}$  and the flattened zone is  $\sim 1100$  km s $^{-1}$ . The high velocity necessary for creation of the "wings" detected in the Ne IX image are more than twice the expansion speed of the nova shell detected in the other wavelengths and about the same in the SW region which is the flattened zone. This shows that the ejecta material is mixed in the forward shock. Using the extensions above and the law of cosines, the cone angle is calculated to be  $\sim 74^\circ$ . The axis of the cone is in the same direction with the axis of the polar cones attributed from the material lying in the light-echo region (Seaquist et al. 1989).

The reverse shock regions are prone to formation of knots because of Rayleigh-Taylor instabilities. The width of the interaction region between the forward and reverse shocks shrinks considerably with increasing compression ratio (due to existence of nonlinear diffusive particle acceleration) and the convective instabilities can reach all the way into the forward shock. As a result, clumps and filaments can be found in the vicinity of the forward shock region. For low compression ratios, any enhancement of the radial magnetic field could play the same role and Rayleigh-Taylor instabilities can still extend all the way into the shock front (see also Blondin & Ellison 2001 for a discussion). This explains the existence of knots of emission (neon knots) in the forward shock zone of GK Per and also mixing of the ejecta material into the forward shock. However, this does not necessarily account for the large asymmetry detected in the remnant.

Therefore, a contributing factor to the above argument for the structure in the emission line would be the existence of undecelerated, cool and dense neon knots in the shell that have caught up with the forward shock and surpassed it in SE and NW directions where the interstellar density is low. Such a phenomenon was also suggested for the knots in Cas A, Vela, Cygnus Loop and others. The SE-NW direction is also the site for the reflection nebula, the symmetric far-IR emission nebulosity, and suggested to be a region of low density (Lawrence et al. 1995; Tweedy 1995; Bode et al. 1987; Seaquist et al. 1989). This is also supported by the CO map of the vicinity of the nova which shows a relatively empty environment toward the north and east of the nova and a prominent CO emission toward the south (Hessman 1989; Scott et al. 1994). Moreover, detected neon clumps could be formed at an early stage in the eruption of the nova and matter could be ejected as knots in



high velocity winds during the early outburst stage (Shore et al. 1997). This also implies a binary orientation origin for the asymmetry in the remnant together with the non-uniform density profile of the circumstellar medium around the nova.

In addition to the Ne IX emission line image, other possible emission line images were constructed at around 0.58 keV (O VII line) and 0.43 keV (N VI line). The resulting images indicate that the shape of the nebula at these energies do not indicate a special structure and the wings seen in the neon image are not detected. Further energy dependence within the X-ray nebula is investigated by constructing images at different energy bands. Figure 9 displays the image of the X-ray nebula in three different energy ranges: (a) 0.25-0.50 keV, (b) 0.51-1.50 keV, and (c) 1.51-8.0 keV. The first two images show emission from the X-ray nebula that is  $2\sigma$  above the background at  $1''$  per pixel resolution, smoothed using a Gaussian with a variable width  $\sigma=1''$ - $2''$ . They are also corrected for the contamination caused by the ACIS transfer streak and the PSF wings as described in sec. (4.1). All three bands indicate different structure. The first two bands (up to 1.5 keV; Figure 9a,b) show generally a filled semi-circular structure brighter on the western side with the brightest zone at the flattened rim which is more evident in the second band. This resembles the structure of the total band image (see Figure 1) except for the "wing" structure detected predominantly in the neon emission line (seen also in the second band image). The second band image is more cone-like owing largely to the motion of the neon knots as described in the previous paragraphs. The third band (hardest X-rays) image is partially resolved (detected spectrally in sec. 4). The original discovery of the X-ray nebula of GK Per was also at a resolution of low significance with the ROSAT HRI between 0.2-2.4 keV (see Figure 1 in Balman & Ögelman 1999). The Chandra observation has recovered most of the emission and structure missed out by the ROSAT HRI, however, the emission above 2 keV is still not completely resolved, but resembles the structure of the ROSAT HRI detection and, also, Figure 9a. Figure 9d is constructed to stress the resolved emission regions at and above  $3\sigma$  confidence level with a lower resolution of  $3''$  per pixel. It is smoothed using a Gaussian with a width of  $\sigma=6''$ . The most prominent region revealed in Figure 9d in the 1.51-8.0 keV band is ellipsoidal with a major axis of  $55''$  and a minor axis of  $27''$  coincident with the brightest region of the shell in 0.2-1.5 keV range as shown by the overlay of contours in Figure 9d. Part of this elliptical emission zone is also the region where the Peak Spectrum is derived and the non-thermal X-ray emission is detected. The different structures in the three different energy bands support that the X-ray emission from the shell of GK Per has different components.

### 6.1. Comparisons with other Wavelengths

In order to investigate the conditions within the shell and determine the evolutionary stage of the remnant, spectral and spatial comparisons in different wavelengths are necessary. Detailed results from the recent data on GK Per are not available. However, a preliminary comparison of the X-ray image has been made by *aligning* the image with the recent images obtained in the optical and radio wavelengths. Figure 10a shows the X-ray image and an overlay of contours derived from the HST image obtained with the [NII] filter (brightest emission line in the optical wavelengths) (HST image: Shara 2002, private communication). The combined image reveals that the [NII] knots and filaments are in general coincident with the central circular region of the X-ray nebula, not with the "wings" detected predominantly in the Ne IX image (see also Figure 9). Both images do not show a well developed shell and are brighter on the Western hemisphere rather than the East. This is not an effect of the X-ray absorption since the spectral fits do not yield significant variation in the  $N_H$  parameter in different directions within the nebula. In general, the [NII] image is larger toward the SW of the nova which indicates cooling in the forward shock and that the remnant has evolved in comparison with the aligned images in Seaquist et al. (1989). The optical shell, mostly composed of knots and filaments, suggests large-scale density gradients in the vicinity of the classical nova. Though the contours look circular in geometry, the HST data indicates an elliptical velocity gradient in the shell with the fastest material lying in the NW to SE direction (Shara 2002, private communication), which is the direction the elongation in the X-ray nebula lies, as detected in the image of the Ne IX line and Figure 9b.

Since there is X-ray emission both from the reverse and forward shocks, the line emission in the UV and optical wavelengths coming from within the shell and the pre-shock zone should be affected by the ionization due to X-ray irradiation (i.e., particularly, the luminosity and evolution of the  $H\alpha$  emission line; Chevalier & Fransson 1994; Chevalier & Oishi 2003). The [OIII] emission line is a characteristics of the shock zones in circumstellar interaction, however the [OIII] emission from the shell is weak and mostly suppressed in the SW region where the X-ray emission is the brightest (Seaquist et al. 1989; Slavin et al. 1995). This could be because the expanding shell is stopped very efficiently and the shock speeds are low in this region (shifting the emission to NII and  $H\alpha$  lines). The densities of the optical knots in the SW are also detected to be high in comparison with the ones in the NE, SE and NW, thus the prominent emission lines are that of [NII] and  $H\alpha$  (Seaquist et al. 1989).

The image of the X-ray nebula has been aligned also with a recent VLA image obtained at 1.425 GHz in 1997 (VLA image: Seaquist 2002, private communication). Figure 10b shows the X-ray image of the shell with an overlay of radio contours. The radio image is mostly circular in structure coinciding with the central circular part of the X-ray nebula

and is slightly smaller than the X-ray image (as compared at a level of  $2\sigma$  emission, see also Balman 2002a). The flattening on the SW is evident in both images. An intriguing result of this combination image is that the peak of the non-thermal radio emission falls slightly offset toward inside of the shell from the brightest X-ray region (X-ray peak of the nova shell). This indicates that the particle acceleration could be occurring at the reverse shock zone consistent with the high absorption associated with the non-thermal X-ray component (see section 5.0). In addition, the outer ridge of the radio shell falls in the X-ray bright zone, as well. An example similar to this has been detected in the *Chandra* observation of the young supernova remnant 1E 0102.2-7219 (Gaetz et al. 2000). Moreover, in Figure 10b the radio wavelength contours show a trace of the "wings" at a  $1.5\sigma$  confidence level (Figure 8, see also the second band image in Figure 9). The part of the radio wavelength (1.425 GHz) image associated with the "wings" seems to be a part of a much larger and fainter emission which may not be associated directly with the shell, but the circumstellar/interstellar environment of the nova. It extends from NW to SE which is in accordance with the lower circumstellar density region and the location of the PN and/or the reflection nebulosity mentioned earlier. The content of the radio spectrum along the "neon wings" is at this time unknown.

## 7. DISCUSSION

### 7.1. On the Origin of the X-ray Nebula

In general, the *Chandra* observation of the shell of nova Persei (1901) has revealed that the remnant evolves similar to the young supernova remnants expanding into its circumstellar medium, a leftover wind ejecta expelled in the course of the binary evolution, and a CO enhanced interstellar medium in the vicinity (similar to Type II SNRs: Chevalier & Fransson 1994 hereafter CF94; see also Truelove and Mckee 1999 for a general review). A conspicuous interpretation of the spectrum of the nova shell is such that the origin of the emission below 2 keV is partly of the ejecta (e.g., Ne and N emission lines) and the circumstellar matter, namely the forward shock (also the transition zone), whereas the emission above 2 keV is of the reverse shock region (owing to the absorption by high equivalent neutral column density).

There is significant difference ( $3\sigma$ ) between the neutral Hydrogen column densities of the two components of the nova shell spectrum. This could be explained in the context of SNR evolution where such a cool layer may exist between the forward and the reverse shocks in the early phases. The size ( $\Delta r$ ) of this cold shell is less than  $5 \times 10^{12}$  cm (less than 0.0005 arc seconds at 470 pc distance) for an SNR 100 years old (CF94), with a range of density  $2 \times 10^8$  to  $3 \times 10^{11}$   $\text{cm}^{-3}$  (CF94). Multiplying the density range with the possible size of this region yields a value of  $N_H$  in the cold shell in a range  $1 \times 10^{21}$ - $2 \times 10^{24}$   $\text{cm}^{-2}$ . The column density

in the cool layer decreases with time and can be expressed as  $N_{cool} \simeq 9 \times 10^{22} (n-4) (t/11.57 \text{ days})^{-1} \text{ cm}^{-2}$  (FLC96). I have assumed  $1200 \text{ km s}^{-1}$  for the expansion speed, a power law index of 2 for the circumstellar density gradient, an  $\dot{M} = 1 \times 10^{-5} M_{\odot} \text{ yr}^{-1}$  for the circumstellar wind and a wind velocity of  $10 \text{ km s}^{-1}$ . For a range of  $n$  from 10 to 200 ( $n$ =power law index for the density gradient in the ejecta), 99 years of age yields  $N_H \simeq 1.2 \times 10^{20} - 8.7 \times 10^{21} \text{ cm}^{-2}$  in the cool layer. SNRs at the age of 100 yrs are about 2 pc in radius (4 pc in size) whereas the radius of GK Per is only 0.11 pc. The size of an SNR at the same evolutionary age with GK Per is larger by a factor of 20 at the least. Thus, time may disperse a cool shell between the forward and reverse shocks in SNRs of high velocities and large sizes, but, since GK Per is considerably slower (compared with an SNR 100 years old) and more compact with respect to an SNR at the same evolutionary age, this cool absorbing layer could stay intact. Moreover, the size of GK Per is equivalent to an SNR a few years old. In such cases, a distinct cool layer is likely (if the reverse shock is radiative) and the emission from the reverse shock would be absorbed.

The high X-ray absorption detected for the shell of GK Per between 0.5-2 keV is not largely due to the neutral hydrogen, but to the neutral metals owing to the fact that the absorbing layer is the cooled part of the reverse shock/ejecta itself. The composition of the ejecta is enhanced in metal abundances of N, Ne and possibly O. Even the circumstellar wind material is at least of solar composition. The absorptivity per hydrogen atom greatly increases above 0.1 keV due to the existence of metals like N, O, Ne, and Fe of solar abundances (Wilms, Allen & McCray 2000 and references therein) which would yield large equivalent column densities of neutral hydrogen. The photoelectric absorption cross-section  $\sigma_K \propto Z^5$  ( $Z$ =atomic number) and the optical depth increases since  $\tau \propto \sigma_K N_H$ . In order to check this, the same composite models in the Tables 1, 2 and 3 are fitted using the multiplicative models VARABS and VPHABS (Balucinska-Church & McCammon 1992) in XSPEC to model the absorption in the second component. These models allow calculation of equivalent column densities of neutral Hydrogen together with elemental abundances of the absorbing medium. The results show that the X-ray data is consistent with a range of equivalent neutral Hydrogen column density of  $5.0_{-2.9}^{+19.0} \times 10^{22} \text{ cm}^{-2}$  attained by, in general, a plasma of solar abundances with  $N/N_{\odot} = 10.9_{-9.1}^{+15.0}$  and  $Ne/Ne_{\odot} = 17.9_{-6.0}^{+9.1}$ . The elemental abundances determined from the cool layer are slightly higher (esp. N) than what is recovered from the analysis of the first component which is the forward shock mixed with the ejecta. Assuming that the cool layer portrays a better representation of the ejecta, then the elemental abundances of Ne and N could be higher than displayed on Tables 1 and 3. The total column density of metals causing the absorption in the cool shell is estimated as  $N_Z < 2 \times 10^{20} \text{ cm}^{-2}$  which yields a total mass in the cool layer of  $M_{coolshell} < 1 \times 10^{-6} M_{\odot}$  (less than 1.5% of the ejecta mass).

The reverse shock speed (using the temperature derived for the second component) is found as  $872 \text{ km s}^{-1}$  and the temperature of the first component (forward shock) implies shock velocities of  $400 \text{ km s}^{-1}$  for the forward shock calculated using the general relation  $kT_s = (3/16)\mu m_H(v_s)^2$ , assuming Rankine-Hugoniot jump conditions in the absence of cosmic-ray acceleration. The average expansion speed detected for the nova is about  $1200 \text{ km s}^{-1}$  in the optical and UV wavelengths (see also sec 1). This value is consistent with the values obtained by measuring the size of the X-ray nebula in the SW direction (see section 6.0), but inconsistent with the speeds calculated for NW and SE directions (see section 6.0). The shock speed calculated using Rankine-Hugoniot jump conditions for the first component associated with the forward shock is also not in accordance with the expansion speed of the shell, at all.

The reverse and forward (circumstellar) shock temperatures scale with  $T_{rev} = ((3 - s)^2 / (n - 3)^2) T_{cs}$ , where  $s$  is the power law index of the circumstellar density gradient and  $n$  is the index for the radial dependence in the ejected material as noted earlier (FLC96). Following this, the ratio of the forward and reverse shock temperatures for the nova remnant are about 4-16 and the shock velocities are about 2-4 (i.e.  $s=1-2$  and  $n=7$ ). As discussed in the previous paragraph,  $n$  is larger than 8 (for a radiative reverse shock) and thus the actual contrast between the forward and reverse shock temperatures are expected to be larger than the above value. This approximation yields a minimum estimation of about  $1600-3200 \text{ km s}^{-1}$  for the forward shock speed ( $\sim 8 \text{ keV}$ ) using the computed reverse shock velocity. There is no component detected in the X-ray spectrum with the stated shock speed range above and the corresponding temperature. *Therefore, the X-ray temperatures does not follow from the shock speeds/expansion speeds as expected from simple shock evolution.* Some of the detected electron temperatures for the blast wave interaction region in young SNRs are found to be as low as  $\sim 10^{6-7} \text{ K}$  (e.g., 1E 0102.2-7219: Hughes et al. 2000, Ellison, Slane & Gaensler 2001; Kepler: Decourchelle et al. 2000; SN 1006: Bamba et al. 2003). This range of shock temperatures are at least a factor of 10 less than what would be expected from such young SNRs. Recent theoretical calculations show that the existence of nonlinear diffusive shock acceleration (particle acceleration at the shock zones) modifies shocks, changing their structure and evolution (Decourchelle et al. 2000; Ellison, Decourchelle & Ballet 2004 and references therein). The particle acceleration at the shock zones (forward or reverse shocks) causes the Mach number to decrease in the post-shock (i.e., sub-shock) regions making the shocked gas more compressible (increasing the compression ratios) resulting in a transition region between the reverse shock and the forward shock that is narrower and denser. As the efficiency of the acceleration increases, the post-shock temperature (esp. for protons) cools significantly (e.g., factor of 10; Ellison et al. 2004 and references therein). Therefore, existence of particle acceleration modifies the shocks and Rankine-Hugoniot conditions are

no longer valid. Consequently, the low temperature (0.1-0.3 keV) and the inconsistent shock speed ( $400 \text{ km s}^{-1}$ ) calculated for the first component of the entire shell spectrum associated with the forward shock could be well explained by nonlinear diffusive shock acceleration. It is important to note that the higher densities and lower temperatures will also lead to more rapid Coulomb equilibration than expected in cases without acceleration.

Considering both of the components and derived electron densities in sections (4.3) and (4.4), the mass in the X-ray emitting nebula is estimated as  $(2.1-38.5) \times 10^{-4} M_{\odot}$  using the simple relation,  $M_{shell} \simeq n_e m_H V_{eff}$ . The calculated shocked mass is consistent with the ejecta mass expected in classical nova explosions (see sec[1]) and the range is 10-50 times the ejecta mass. The expansion speed for nova Persei 1901 yields a total kinetic energy of  $(1.1-6.2) \times 10^{45}$  ergs for the ejecta ( $1/2 M_{ej} v_{ej}^2$  and for  $M_{ej}$  and  $v_{ej}^2$  see the Introduction). The total explosion energy of a classical nova event is of the order of  $10^{46}-10^{47}$  ergs (i.e., binding energy of the envelope of the white dwarf;  $E_0 = 2GM_{WD}M_{env}/R_{WD}$ ). Assuming that the shell will be radiative at the time maximum X-ray luminosity is reached, then  $L_{max} \simeq E_0/t_{max}$ . If  $t_{max}$  were 99 years (time since the eruption), we can calculate that  $L_{max} \simeq 10^{37-36}$  ergs  $s^{-1}$ . The kinetic energy dumped in the ejecta (about 1% of the total explosion energy) translates to about  $L_{max} \simeq 10^{35}$  ergs  $s^{-1}$  for a radiative shell. The reverse shock luminosity is expected to decrease in time by a factor of 100-1000 times after 100 yrs (CF94) and the luminosity should be, then, in a range  $10^{33-32}$  ergs  $s^{-1}$  which is in accordance with the detected luminosity of the second component (the reverse shock;  $L_x = (6.6-0.14) \times 10^{33-32}$  ergs  $s^{-1}$ ). On the other hand, given the low luminosity of the shell originating in the forward shock a few  $\times 10^{32}$  ergs  $s^{-1}$  and the fact that the calculated maximum shocked mass is larger than the ejecta mass, the remnant is most likely evolving in the Sedov phase as an adiabatic remnant.

It is of evolutionary importance to note that the environment of GK Per resembles the class of SNRs that interact with molecular clouds (Seaquist et al. 1989). The Figure 1 and 9 reveals that the shell has a lumpy structure which could, also, support the existence of cloud crushing; shocks with the molecular clumps (White & Long 1991). A part of the emission of the second component could be due to this. Interactions of SNRs with dense environments have been modeled and old remnants like W44 and IC443 are recovered as the candidates for such SNR evolution with a colder radiative shell in the X-rays and a hot isothermal gas around 1 keV at the center (Rho & Petre 1998; Shelton et al. 1999; Chevalier 1999; Bykov et al. 2000). The modeling of SNR W44 (interacting with a dense inhomogeneous region in the vicinity of a molecular cloud) yields a one sided X-ray emitting hemisphere, a hot interior and a colder radiative shell as modeled by Cox et al. (1999). This has a remarkable resemblance in *structure* to the remnant of GK Per except that the outer shell is not radiative and cold due to age, but rather adiabatic and cold most likely as an effect of the particle acceleration and modified shock evolution. Overall, the nova remnant of GK Per could be a

younger remnant that will eventually resemble older remnants like W44 or IC443.

The photon emission in the X-ray wavelengths presumably arising from the accelerated particles could be a non-thermal bremsstrahlung process resulting from a particular non-Maxwellian distribution of accelerated electrons (Asvarov et al. 1990) or synchrotron emission from a power law distribution of such electrons. The non-thermal synchrotron emission from the nova remnant as reported in section (5.0) is coming from the brightest X-ray emission region which is most likely an X-ray filament. Lately, such non-thermal filaments have been recovered in SNRs with similar photon indexes in a range 2.1-2.5 (e.g., Bamba et al. 2003; Uchiyama et al. 2003, Ueno et al. 2003). The spectrum of accelerated particles in the X-ray band should be highly sensitive to the local neutral density and have a non-thermal/thermal bremsstrahlung component at high  $n_0$  for hard X-ray emission. The non-thermal bremsstrahlung intensity is  $1.0 \times 10^{15} n N_0 E^{-\Gamma} / (\Gamma - 1) \text{ cm}^{-3} \text{ erg}^{-1} \text{ s}^{-1}$  (cf. Chevalier 1999). The emission from radio to the X-ray band is dominated by synchrotron emission from energetic electrons for  $B > 10 \mu\text{G}$  with bremsstrahlung dominating X-rays for  $B \leq 3 \mu\text{G}$  (see discussion in Ellison, Berezhko, & Baring 2000 and Ellison et al. 2004 for more details). The estimations on the circumstellar magnetic field intensities in the non-thermal radio peak region and the following outer ridge of GK Per are 75 and 47  $\mu\text{G}$ , respectively (Seaquist et al. 1989). As a result, one expects a synchrotron X-ray emitting region co-spatial with the peak and outer ridge detected in the radio wavelengths of GK per as presented in this paper.

The X-ray luminosity and the power law index from the brightest X-ray (peak) region can be used to determine the non-thermal electron density and the total energy in the accelerated electrons. The accelerated electron population will have a distribution in basic terms  $N_e(E) = K E^{-s}$  with an individual electron losing energy via synchrotron process as

$$-\dot{E} = \frac{4}{3} \sigma_T c \left( \frac{E}{m c^2} \right)^2 \left( \frac{B^2}{8\pi} \right), \quad (3)$$

averaging over all pitch angles and taking electron velocity  $\sim c$ , where  $\sigma_T$  is the Thomson cross-section. The electron distribution described above will have a multiplicative exponential decay term to explain the age-limited, and necessarily the loss-limited or escape-limited SNRs more properly (see Reynolds 1998 and references therein). Following from the prescriptions of Reynolds (1998), the ratio of the maximum electron energy for the remnant of GK Per and the theoretical energy (i.e.,  $E_f$  in eq. 27 and 26 of Reynolds (1998)) of an initially infinitely energetic electron in the same magnetic field (as in the remnant of GK Per) radiating for the same duration time  $t$  predicts that the remnant is age-limited (young for synchrotron losses to dominate or particle escape to be prominent).

The injection efficiency for the remnant ( $\eta = n_{non-thermal} / n_{thermal}$ ) is proportional to the ratio of the electron number densities of the non-thermal and thermal electrons. I estimate

that  $\eta = 1.4 \times 10^{-3}$  for the brightest X-ray (peak) region of the remnant of GK Per. This is about the same order of magnitude with the  $\eta$  reported for SN 1006 (Bamba et al. 2003) which is the most efficient SNR known to accelerate particles to very high energies close to the knee. The non-thermal electron density is calculated as  $n_{non-thermal} = 3.01 \times 10^{-3} \text{ cm}^{-3}$  for a filling factor of 1 ( $n_{thermal} = 2.0 \text{ cm}^{-3}$  for  $f=1$ ). A basic power law electron distribution is assumed for the calculation, along with the integration limits : (1) a minimum energy (the injection energy) of 1 keV (the temperature of the thermal plasma of the second component), (2) a maximum energy of 15 TeV. In accordance with the photon extraction region, a volume of  $2.8 \times 10^{52} \text{ cm}^{-3}$  is also, assumed.

The non-thermal energy density of the brightest X-ray emission (peak) region is estimated as  $3.0 \times 10^{-10} \text{ erg cm}^{-3}$ . This is calculated using the same integration limits and volume described in the above paragraph together with a distribution of power emitted by the given power law electron distribution (i.e.,  $[dP(E)/dE] \simeq \dot{E}[dN(E)/dE]$ ). The corresponding energy densities of the magnetic field and the thermal plasma are  $2.3 \times 10^{-10} \text{ erg cm}^{-3}$  ( $u_B = B^2/8\pi$ ) and  $5.1 \times 10^{-9} \text{ erg cm}^{-3}$  ( $u_{thermal} = 3/2 n_e kT$ ), respectively. The energy densities are a factor of 10 higher compared with SN 1006 by Bamba et al. (2003). The total energy in the thermal plasma, the magnetic field and the non-thermal electrons are then,  $2.2 \times 10^{45}$  ergs,  $9.5 \times 10^{43}$  ergs (if total volume is assumed and  $6.2 \times 10^{42}$  ergs if the photon extraction region is assumed), and  $1.2 \times 10^{44}$  ergs (if total volume is assumed and  $8.4 \times 10^{42}$  ergs if the photon extraction region is assumed), respectively. As a result, the magnetic field is almost/in equipartition with the non-thermal electrons (taking that these calculations are estimations). The non-thermal protons should carry more energy than the non-thermal electrons (in a range 1-2000 times the total energy of electrons [ $2000 \sim m_p/m_e$ ]).

There are strong indications of possible nonlinear diffusive particle acceleration occurring in the forward shock zone as well as the reverse shock zone; (1) the unexpectedly cool X-ray temperature, (2) the strongly compressed interaction region between the forward and reverse shocks where the ejecta material is detected to be mixed in. However, including a second power law or SRCUT model of emission in the fits applied on the X-ray data below 2 keV does not yield physical or statistically consistent results unless the first component is fitted with a bremsstrahlung model and three Gaussians for emission lines along with the SRCUT/power law model. Inclusion or exclusion of the SRCUT/power law model does not affect the reduced  $\chi^2$  of the fits. Thus, an upper limit on the non-thermal X-ray flux from the forward shock is  $F_x < 1.0 \times 10^{-14} \text{ erg s}^{-1} \text{ cm}^{-2}$  with a photon index of  $2.8_{-2.5}^{+4.4}$  and a luminosity  $< 3.0 \times 10^{29} \text{ erg s}^{-1}$ . The SRCUT model implies a radio spectral index of  $0.8_{-0.1}^{+0.2}$ . There can be several explanations for this: (a) the energy going into particle acceleration is less, (b) the synchrotron losses and/or particle escape is more effective compared with the reverse shock yielding a lower X-ray flux for the forward shock zone, (c) the forward shock



is under-ionized as discussed in section (4.3) which results in a lower injection efficiency and thus less particles in the non-thermal regime. Ellison et al. (2004) shows that nonlinear diffusive shock acceleration in the forward and reverse shocks could evolve differently. The emission from the reverse shock may increase out to 1000 years and the efficiency diminishes after that together with the luminosity. The emission and efficiency from the forward shock is expected to increase slowly out to 40000 years and may be small for young SNRs (younger than 1000 yrs).

## 7.2. The Classical Nova Remnants

The studies of resolved old nova shells provide an opportunity of investigating several facts of the evolution of novae long after the initial eruption has subsided. Spectroscopy and imaging of the nebular remnants of old novae have been a diagnostic of physical conditions in (mode of excitation) and the morphology of the nova shells. Optical spectroscopy/imaging of nova shells has been widely used for this purpose. By direct imaging method, the ejecta of several old novae have been spatially resolved with evidence/detection of polar blobs and equatorial rings in many of them (Slavin et al. 1995; Gill & O’Brien 1998, 2000; Krautter et al. 2002; Bode 2002 and references therein). The expansion velocities of material in a nova shell are suggested to vary smoothly as a function of position angle from a maximum in the polar regions to a minimum at the equator, which results in a prolate asymmetry (Lloyd et al. 1997). In addition to this, abundance gradients are expected as a result of TNRs (Thermo-Nuclear Runaway) in rotating oblate white dwarfs as detected from observations (RR Pic, DQ Her, V1370 Aql, V838 Her, etc.; Scott 2000). Recently, the HST imaging of HR Del indicates several emission knots in [OIII], [NII] and  $H\alpha$ ; particularly a bipolar structure in the first two compared with the latter (Harman & O’Brien 2003). Analysis of HR Del reveals that there are also indications of wind (from the central source) interaction with the old remnant shell affecting its evolution and structure. In general, optical and UV wavelength measurements of electron temperatures in the nova shells indicate two groups of old remnants; hot ( $T_e > 10^4$  K) and cold ( $T_e < 10^4$  K) nova shells (Williams 1992, Ferland 1984). Some of the nova shells have been found to decelerate in time, such as DQ Her, GK Per, V603 Aql, T Pyx, and V476 Cyg, suggesting the existence of circumstellar interaction (Duerbeck 1987).

The first prediction of classical nova remnants as non-thermal radio sources has been made by Chevalier (1977). However, there have not been any X-ray or radio wavelength (Bode et. al. 1987) detections of old classical nova remnants except for GK Per. The detailed theoretical framework on the hydrodynamical shock evolution in classical nova remnants

is being developed (See Bode 2002 for a review). The circumstellar interaction has been modeled for recurrent novae (RS Oph: Bode & Kahn 1985; T Pyx: Contini & Prialnik 1997). These models (esp. for T Pyx) predict the existence of a forward moving blast wave and a reverse shock moving into the ejecta as a result of colliding shells from the eruptions. Their model also predict a cold layer of material between the forward and reverse shocks (they do not study it in detail). The models indicate high electron densities of the order of a few hundred  $\text{cm}^{-3}$  in the shock zones. Another intriguing result from these studies is that the magnetic field is enhanced by factors of 10 to 100 due to instabilities and turbulent motion.

The power from a simple shocked-shell model of thermal origin, as an X-ray emitting nebula, can be modeled assuming a 0.25 filling factor for the volume of the shell (assumed to be spherical) and  $n_e \sim 4n_o$  (from strong shock conditions);

$$L_T \simeq 3.1 \times 10^{33} T_7^{0.5} n_o^2 R_{18.5}^3. \quad (4)$$

The temperature T is in units of  $10^7$  K and the radius of the emitting shell R is in units of  $3.1 \times 10^{18}$  cm. The fast nova ejecta will start to cool as it sweeps up an equal amount of circumstellar material at  $R_{cool}$  and  $t_{cool}$ . Once it sweeps up about 10 times its own mass, it will proceed into the Sedov phase;

$$R_{cool} \simeq 0.03(M_{-5}/n_o)^{1/3} pc, \quad (5)$$

$$t_{cool} \simeq 30(M_{-5}/v_{1000}^3 n_o)^{1/3} yrs, \quad (6)$$

$$t_{Sedov} \simeq 64(M_{-5}/v_{1000}^3 n_o)^{1/3} yrs. \quad (7)$$

For  $n_o \simeq 0.1-10 \text{ cm}^{-3}$ ,  $kT \simeq 0.1-10 \text{ keV}$  and  $R \sim R_{cool}$ , the range of X-ray luminosity is a few  $\times 10^{34}$  to a few  $\times 10^{28} \text{ ergs s}^{-1}$  as the remnants start to cool. Assuming adiabatic remnants (at the onset of cooling), about 1% of this radiation should be detected. Thus, the maximum limit of X-ray emission is then about  $10^{32} \text{ ergs s}^{-1}$  which is in good agreement with the X-ray luminosity of the remnant of GK Per (i.e., brightest remnant). The time to start to progress into the Sedov phase is  $< 96$  yrs for GK Per, calculated using equation (7) which is consistent with the interpretation that the remnant is in the Sedov phase. I would like to note that the X-ray synchrotron emission from the remnant of GK Per is a special case and a result of the circumstellar environment and the magnetic fields.

Theory would expect that the remnants should become fully radiative in the later stages of the shock evolution (i.e. Snowplow phase), increasing the luminosity in excess of  $\times 10^{35} \text{ ergs s}^{-1}$ . However, by that time the remnant will expand to a much larger size where the decreasing surface brightness will affect this evolution and may no longer permit the remnant to be detected.

## 8. SUMMARY AND CONCLUSIONS

The nova shell of GK Per is the first classical nova remnant resolved and detected in the X-ray wavelengths. *Chandra* Observatory has revealed the spectrum and detailed morphology of this remnant for the first time and this has helped to raise/resolve important questions related to classical nova eruptions, hydrodynamic flows and relativistic particle generation. In general, the nova remnant of GK Per evolves similar to young, type II SNRs and a shell is constructed via the interaction of the ejecta with the circumbinary medium which is a leftover wind and/or a Planetary Nebula. The X-ray nebula around GK per is brightest on the SW quadrant and toward West with a lumpy morphology. There is a central semi-circular region and "wing" like extensions toward SE and NW. The central circular region resembles the radio/VLA shell and the optical/HST images with several clumps/knots in the X-rays. Some features are collection of clumps and filamentary structures, also, indicating radial elongations.

The X-ray shell has a symmetric cone-shaped structure detected in a Ne IX emission line with a cone angle of about  $74^\circ$  to the central source which indicates the shock front. The shell is most likely expanding into a less dense medium in the NW and SE directions which comprises the "wings" with speeds (i.e.,  $2600 \text{ km s}^{-1}$ ) more than twice the expansion speed in the SW direction (i.e.,  $1100 \text{ km s}^{-1}$ ). The VLA/radio image of the remnant shows a trace along the "wings" detected in the X-rays as part of a larger diffuse radio emission stretching from NW to SE in the direction of the reflection nebulosity. The neon line emission and the neon wings detected toward the NW and SE, moving with speeds  $\sim 2600\text{-}2800 \text{ km s}^{-1}$ , originate from the clumped ejecta due to instabilities in the post-shock region. Such knots are expected to transit into the forward shock zone in time with possibly the aid of a circumstellar magnetic field and compression of the interaction region due to the effects of nonlinear diffusive shock acceleration (particle acceleration). It is also possible that some of these knots could have been created within the remnant or even at the onset of the nova explosion and have not significantly decelerated, eventually surpassing the shock zone particularly in the NW and SE directions where the interstellar density is low. The NE portion of the circumstellar environment does not show a distinct sign of interaction (i.e., a bright rim) as in the SW and lacks line emission. In general, X-ray nebula is the largest among the detected radio and optical shells. The shape of the X-ray nebulosity is a combination of the characteristics of the circumstellar medium around the nova and the geometrical projection effects that requires a special treatment with hydrodynamical models. Creation of a hemispherical X-ray shell, as detected for GK Per in this paper, is theoretically expected in regions with high ambient density gradients as revealed by studies in SNRs evolving in molecular clouds (e.g. W44, Cox et al. 1999).

The nova shell of GK per is a site where energetic electrons are produced by diffusive shock acceleration (particle acceleration) confirmed by the *Chandra* observation via the discovery of the synchrotron emission from the non-thermal electrons in the reverse shock zone. The detected power law emission in the X-rays reveals the same spectral index as in the radio wavelengths recovered with the fits using a SRCUT model of emission. The detected X-ray photon index is  $2.3_{-0.9}^{+1.5}$ , the spectral index is  $0.68_{-0.15}^{+0.03}$  and the unabsorbed luminosity is  $4.6 \times 10^{30} \text{ erg s}^{-1}$ . The remnant is age-limited. The non-thermal electron density is about  $3.01 \times 10^{-3}$  ( $f=1$ ) and the efficiency of injection in the reverse shock is about  $1.4 \times 10^{-3}$ . This value is similar to the efficiency derived for SN 1006 which is the most efficient SNR in particle acceleration. However, the derived luminosity for GK Per is lower because the emitting volume is smaller. The cool X-ray temperature (0.1-0.3 keV) of the forward shock indicates that there is nonlinear diffusive shock acceleration occurring in this region, also. However, the efficiency and the luminosity is low ( $L_x < 3 \times 10^{29} \text{ erg s}^{-1}$  and  $\Gamma > 2.8$ ) and can not be resolved from the thermal emission. This complies with the theoretical expectations that for young SNRs the contribution from particle acceleration into the energetics of the systems will be small.

The calculated break frequency for the remnant shows that GK Per is also a strong candidate for gamma-ray emission (out to the knee) due to the accelerated particles in the reverse shock region with  $E_{max}$  about 15-30 TeV (this should be more or less correct for the forward shock region, too).

The X-ray nebula has a low temperature component (below 2 keV), the first component, that is a (non-equilibrium ionization) thermal plasma close to ionization equilibrium, possibly dominated by emission lines, with  $kT \sim 0.1\text{-}0.3 \text{ keV}$  and an X-ray luminosity  $\sim 4.3 \times 10^{32} \text{ ergs s}^{-1}$ . This component shows the He-like Ne IX (i.e, most contribution may be coming from a forbidden emission line) and He-like N VI line emission derived from the spectral fits (and a possible O VII emission line). No H-like line emission is detected. This component is associated with the forward shock region and the transition zone owing to the low neutral Hydrogen column density. Thus, it is a mixed plasma of shocked circumstellar matter and ejecta material. The electron density within this region is  $0.6\text{-}11.2 \text{ cm}^{-3}$  (for a filling factor of 1). The  $n_0$  in the circumstellar medium is  $\leq 60 \text{ cm}^{-3}$  ( $n_0 \sim 4.1 \text{ cm}^{-3}$ ).

The higher energy component of the entire shell spectrum above 2 keV is most likely a plasma emission of bremsstrahlung origin with no resolved emission lines. The fits using a thermal bremsstrahlung model of emission reveal a shock temperature of  $kT = 1.04_{-0.5}^{+1.7} \text{ keV}$  and an X-ray luminosity  $(6.6\text{-}0.14) \times 10^{33} \text{ erg s}^{-1}$ . It is found to be heavily absorbed with  $N_H = (4.0\text{-}22.0) \times 10^{22} \text{ cm}^{-2}$  suggesting that there is a cold layer of material between the two X-ray components and the second component is most likely originating from the shocked gas

in the reverse shock zone. The X-ray analysis reveals that this cold layer is a plasma of solar abundances with  $N/N_{\odot} \sim 11$  and  $Ne/Ne_{\odot} \sim 18$  where the high metallicity of the ejecta in this cooling layer is largely responsible for the high optical depth between 0.2 and 2 keV. It is also important to note that this high column density of neutrals absorbs the emission below 1.5 keV where most of the line emission would be detected.

The standard nova theory predicts enrichment of metal abundances produced prior to the outburst via mixing processes. This observation reveals for the first time a minimum enhancement of neon 13-21 and nitrogen 1-5 times its solar number fraction from a remnant in the X-rays that is 100 yrs old. Moreover, the existence of enhanced neutral abundances of neon and nitrogen in the "cold absorbing shell" supports this finding. As a result, this confirms that the outburst was a result of a violent TNR on an ONeMg WD, which would, also, explain the existence of a blast wave. The high nitrogen ratio is a direct evidence of the  $\beta^+$  unstable nuclei which must have been ejected with the blast wave from the nova in the early stages.

The kinetic energy density of the ejecta is  $(0.3-1.5) \times 10^{-8}$  erg  $\text{cm}^{-3}$  where the maximum limit comes from the calculated shocked mass (i.e.  $(2.1-38.5) \times 10^{-4} M_{\odot}$ ). The energy densities of the thermal plasma, magnetic field and non-thermal electrons are  $5.1 \times 10^{-9}$  erg  $\text{cm}^{-3}$ ,  $2.3 \times 10^{-10}$  erg  $\text{cm}^{-3}$  and  $3.0 \times 10^{-10}$  erg  $\text{cm}^{-3}$ , respectively, implying that the magnetic field and the non-thermal electrons are almost/in equipartition at the shock zone. The energy budget of the nova remnant indicates that not all the kinetic energy has appeared as thermal energy in the shock zone, in accordance with the fact that the remnant is young. Thus, considerable energy is still going into expansion of the shell and about less than 34% appears as thermal energy with about less than 2% in the accelerated particles. The low X-ray luminosity ( $4.3 \times 10^{32}$  erg  $\text{s}^{-1}$ ) of the forward shock indicates that the remnant is adiabatic. The reverse shock is radiative. Overall, the nova shell of GK Per resemble a Sedov remnant (of SNRs). The cooling in the forward shock is also detected in the HST [NII] images (very similar to  $H\alpha$  images) aligned with the X-ray data (see Figure 10a).

The nova shell of GK Per remains to be unique with its characteristics over the entire electromagnetic spectrum. It behaves as a miniature SNR with typical characteristics, yet it is the first detection of CNRs (Classical Nova Remnants), which can be a new class of X-ray emitters that have considerably low surface brightness/luminosity and shocked mass compared with SNRs; as a result evolving faster than, but similar to SNRs. The luminosity range for such objects are between a few  $\times 10^{32}$  to a few  $\times 10^{26}$  ergs  $\text{s}^{-1}$  as the adiabatic remnants start to cool. After the outburst of a classical nova, the typical cooling timescale for the hard X-ray emission components due to wind-wind interactions is about three years (Balman et al. 1998). However, as the shell interacts with its circumstellar environment, it

should produce about the range of luminosity above depending on how strong the shock will be (i.e., density contrast/compression ratio) and how the expansion will affect the surface brightness of the remnant. Two other candidates, DQ Her and RR Pic indicate residual emission coming from the location of their shells (Mukai, Still, & Ringwald 2003; Balman 2002b). Recovering CNRs require simultaneous high sensitivity and spatial resolution and pose a challenge given the characteristics of the present and upcoming X-ray missions. The ACIS detector on *Chandra* and Epic PN on Newton-XMM could discover some of the close-by and luminous CNRs.

The Author thanks E. Seaquist and M. Shara for making the VLA and HST images available before publication. Many thanks, also, to an anonymous referee for the critical reading of the manuscript. I would like to also thank M. Bode, D. Ellison, M. Hernanz, J. Krautter, K. Mukai, H. Ögelman, E. Schlegel, M. Shara, N. Schultz and P. Plucinsky for helpful remarks or help with data handling. This work has made use of *Chandra* archives and *Chandra* workshop (2001)/user help desk on several occasions. Finally, I would like to acknowledge the support from the Turkish Academy of Sciences with the TUBA-GEBIP (distinguished young scientist award) Fellowship.

## REFERENCES

- Asvarov, A.I., Guseinov, O.H., Kasumov, F.K., & Dogel, V.A. 1990, *A&A*, 229, 196
- Balman, S., Krautter, J., & Ögelman, H. 1998, *ApJ*, 499, 395
- Balman, S., & Ögelman, H.B. 1999, *ApJ*, 518, L111
- Balman, S. 2001, in *X-ray astronomy 2000*, ASP Conf. Ser., Vol. 234, R. Giacconi, L. Stella, S. Serio (eds), p. 269
- Balman, S. 2002a, in *X-rays at Sharp Focus: Chandra Science Symposium*, ASP Conf. Ser., Vol. 262, S. Vrtilik, E. Schlegel, L. Kuhl (eds), p. 34
- Balman, S. 2002b, in *Classical Nova Explosions*, AIP Conf. Proc., Vol. 637, Margarita Hernanz & Jordi Jose (eds), p. 365
- Balucinska-Church, M. & McCammon, D. 1992, *ApJ*, 400, 699
- Bamba, A., Yamazaki, R., Masaru, U., & Katsuji, K. 2003, *ApJ*, 589, 827
- Baring, M., Ellison, D., Reynolds, S., Greiner I., & Goret P. 1999, 513, 311
- Barnard, E. 1917, *Astr. Nachr.*, 4869, 375
- Berezhko, E., & Völk, H. 1997, *Astropart. Phys.*, 7, 183

- Berezhko, E., Pühlhofer, G., & Völk, H. 2003, *A&A*, 400, 971
- Biermann, P.L., Strom, R.G., & Falcke, H. 1995, *A&A*, 302, 429
- Blondin, J.M., & Ellison, D.C. 2001, *ApJ*, 560, 244
- Bode, M. F., & Kahn, F. D. 1985, *MNRAS*, 217, 205
- Bode, M. F., Seaquist, E. R., Frail, D. A., Roberts, J. A., Whittet, D. C. B., Evans, A., & Albinson, J. S. 1987 *Nature*, 329, 519
- Bode, M.F., Seaquist, E. R., & Evans, 1987, *MNRAS*, 227, 217
- Bode, M.F. 2002, in *Classical Novae Explosions*, AIP Conf. Proc., Vol. 637, Margarita Hernanz & Jordi Jose (eds), p. 497
- Bode, M.F., O'Brien, T.J., & Simpson, M. 2004, *ApJ*, 600, L63
- Borkowski, K., Szymkowiak, A.E., Blondin, J., & Sarazin, C. 1996, *ApJ*, 466, 866
- Bykov, A., Chevalier, R., Ellison, D., & Uvarov, Y. 2000, *ApJ*, 538, 203
- Chevalier, R. A. 1977, *A&A*, 59, 289
- Chevalier, R. A., & Fransson, C. 1994, *ApJ*, 420, 268
- Chevalier, R. A. 1999, *ApJ*, 511, 798
- Chevalier, R. A., & Oishi, J. 2003, 593, L23
- Contini, M., & Prialnik, D. 1997, *ApJ*, 475, 803
- Couderc, P. 1939, *Ann. d'Astrophys.*, 2, 271
- Cox, D.P., Shelton, R.L., Maciejewski, W., Smith, Randall, K., Plewa, T., Pawl, A., & Rozyczka, M. 1999, *ApJ*, 524, 179
- Decourchelle, A., Ellison, D.C., & Ballet, J. 2000, *ApJ*, 543, L57
- Dougherty, S. M., Waters, L., Bode, M., Lloyd, H. M., Kester, D. J., & Bontekoe, T. 1996, *MNRAS*, 306, 547
- Duerbeck, H.W. 1987, *Ap&SS*, 131, 461
- Ellison, D., Berezhko, E., & Baring, M. 2000, *ApJ*, 540, 292
- Ellison, D., Decourchelle, A., & Ballet, J. 2004, *A&A*, 413, 189
- Episto, J., Hunter, S., Kanbach, G., & Sreekumar, P. 1996, *ApJ*, 461, 820
- Ferland, G. J., Williams, R. E., Lambert, D. L., Shields, G. A., Slovak M., Gondhalekar, P. M., & Truran, J. W. 1984, *ApJ*, 281, 194
- Fransson, C., Lundqvist, P., & Chevalier, R. 1996, *ApJ*, 461, 933

- Gaetz, T.J., Butt, Y., Richard, E., Kristoffer E., Plucinsky, P. Schlegel E., & Smith R. 2000, ApJ, L47
- Gaisser, T., Protheore, R., & Stanev, T. 1998, ApJ, 492, 219
- Gill, C.D., & O’Brien, T.J. 1998, MNRAS, 300, 221
- Gill, C.D., & O’Brien, T.J. 2000, MNRAS, 314, 175
- Garmire, G., Feigelson, E.D., Broos, P., Hillenbrand, L.A., Townsley, L., & Tsuboi, Y. 2000, AJ, 120, 1426
- Hamilton, A.J., Sarazin, C., & Chevalier, R.A. 1983, ApJS, 51, 115
- Hamilton, A.J. 1985, ApJ, 291, 523
- Harman, D.J. & O’Brien, T.J. 2003, MNRAS, 344, 1219
- Harnden, F.R. Jr., Fabricant, D.G., Harris, D.E., Schwarz, J. 1984, SAO Rep., No. 393
- Hughes, J.P., Rakowski, C., & Decourchelle, A. 2000, ApJ, L61
- Kapteyn, J. C., 1901, Astr. Nachr., 3756, 201
- Krautter, J., Woodward, C., Schuster, M., Gehrz, R.,D., Jones, T., Belle, K., Evans, A., Leyers, S.P., Starrfield, S., Truran, J., & Greenhaus, M. 2002, AJ, 124, 2888
- Küpcü-Yoldas, A., & Balman, S. 2002, A&A, 384, 190
- Lawrence, S. S. et al. 1995, AJ, 109, 2635
- Liedahl, D.A., Osterheld, A.L., & Goldstein, W.H. 1995, ApJ, 438, L115
- Livio, M., in *Interacting Binaries*, Saas-Fee Advanced Course 22, ed. H. Nussbaumer & A. Orr (Berlin: Springer), 135
- Lloyd, H.M., O’Brien T.J., & Bode, M. 1997, MNRAS, 284, 137
- Mc Laughlin, D.B. 1960, in *Stars and Stellar systems*, Vol.6, *Stellar Atmospheres* (ed Greenstein, J. L.), (Chicago:University of Chicago Press), 585
- Mewe, R., Gronenschild, E.H.B.M., & van den Oord, G.H.J. 1985,A&AS, 62, 197
- Mukai, M., & Ishida, M. 2001, ApJ, 551, 1024
- Mukai, M., Still, M. & Ringwald, F. 2003, ApJ, 594, 428
- Ness, J-U. et al. 2003, ApJ, 594, L127
- Oort, J.H. 1951, in *Problems of Cosmical Aerodynamics*, p.118, ed. Burgess, J., Central air Documents, Dayton, Ohio
- Orio, M., Parmar, A., Benjamin, Z., Amati, L., Frontera, F., Greiner, J., Ögelman, H., Mineo, T., Starrfield, & S., Trusoni, E. 2001, MNRAS, 326, 13



- Payne-Gaposchkin, C. 1957, in *The Galactic Novae*, ed. J.H. Oort M.G.J. Minaert, & H.C. van de Hulst (New York: Dover), 299
- Pottasch, S. R. 1959, *Ann. d' Ap.*, 22, 412
- Reynolds, S. P., & Chevalier, R. A. 1984, *ApJ*, 281, L33
- Reynolds, S. P., 1998, *ApJ*, 493, 357
- Reynolds, S. P., & Keohane, J. W., 1999, *ApJ*, 525, 368
- Rho, J., & Petre, R. 1998, *ApJ*, 503, L167
- Rho, J., Dyer, K., Borkowski, K.J., & Reynolds, S.P. 2002, *ApJ*, 581, 1116
- Seaquist, E. R., Bode, F. M., Frail, D. A., Roberts, J. A., Evans, A., & Albinson, J. S. 1989, *ApJ*, 344, 805
- Slavin, A. J., O'Brien, T. J., & Dunlop, J. S. 1995, *MNRAS*, 276, 353
- Scott, A.D. 2000, *MNRAS*, 313, 775
- Scott, A.D., Rawlings, J.M.C., & Evans, A. 1994, *MNRAS*, 269, 707
- Shara, M. 1989, *PASP*, 101, 5.D. 2000, *MNRAS*, 313, 775
- Shelton, R.L., Cox, D.P., Maciejewski, W., Smith, R.K., Plewa, T., Pawl, A., & Rozyczka, M. 1999, 524, 192
- Shore, S., Starrfield, S., Ake, T., & Hausschildt, P. 1997, *ApJ*, 490, 393
- Spitzer, L. 1978, *Physical Processes in the Interstellar Medium*, (Newyork: John Wiley & Sons)
- Starrfield, S. 2001, in *ASP Conf. Ser. 231, Tetons 4: Galactic Structure, Stars, and the Interstellar Medium*, C.E. Woodward, M.D. Bica, & J.M. Shull (eds), (San Francisco: ASP), p. 466
- Stunner, S., Skibo, J., Dermer, C., & Mattox, J. 1997, *ApJ*, 490, 619
- Tweedy, R. W. 1995, *ApJ*, 438, 917
- Truelove, J.K., McKee, C.F. 1999, *ApJS*, 299, 120
- Uchiyama, Y., Aharonian, F., & Takahashi, T. 2003, *A&A*, 400, 567
- Ueno, M., Bamba, A., Koyama, K., & Ebisawa, K. 2003, *ApJ*, 588, 338
- Warner, B. 1995, *Cataclysmic Variables* (Cambridge: Cambridge Univ. Press)
- Weisskopf, M., O'dell, Stephen, L., van Speybroeck, L.P., 1996, *SPIE*, 2805, 2
- White, R.L. & Long, K.S. 1991, *ApJ*, 373, 543
- Williams, R. E. 1982, *ApJ*, 261, 170

Wilms, J., Allen, A. , & McCray, R. 2000, ApJ, 542, 914

Table 1: Spectral Parameters of the Entire Spectrum of the Nova Shell for the **Softer X-ray Component in the energy range 0.3-2 keV** (ranges correspond to  $2\sigma$  errors)

	VPSHOCK § <sup>1</sup>	VMEKAL § <sup>2</sup>	BREMSS+3(GAUSSIAN) § <sup>3</sup>
$N_H$ ( $\times 10^{22}$ cm <sup>-2</sup> )	0.30 <sup>+0.07</sup> <sub>-0.07</sub>	0.23 <sup>+0.05</sup> <sub>-0.04</sub>	0.19 <sup>+0.18</sup> <sub>-0.16</sub>
$kT_s$ <sup>a</sup> (keV)	0.11 <sup>+0.04</sup> <sub>-0.02</sub>	0.10 <sup>+0.02</sup> <sub>-0.01</sub>	0.27 <sup>+0.78</sup> <sub>-0.16</sub>
Nitrogen (N/N <sub>⊙</sub> )	3.1 <sup>+1.6</sup> <sub>-2.1</sub>	3.0 <sup>+0.8</sup> <sub>-1.2</sub>	N/A
Oxygen (O/O <sub>⊙</sub> )	1.8 <sup>+1.7</sup> <sub>-0.8</sub>	N/A	N/A
Neon (Ne/Ne <sub>⊙</sub> )	16.3 <sup>+4.6</sup> <sub>-3.4</sub>	9.23 <sup>+6.0</sup> <sub>-1.2</sub>	N/A
$\tau$ ( $\times 10^{11}$ s cm <sup>-3</sup> )	0.3 <sup>+1.4</sup> <sub>-0.2</sub>	N/A	N/A
EM <sup>b,c</sup> ( $\times 10^{53}$ cm <sup>-3</sup> )	138.6 <sup>+408.5</sup> <sub>-111.2</sub>	66.7 <sup>+133.3</sup> <sub>-63.24</sub>	52.1 <sup>+238.4</sup> <sub>-51.9</sub>
Line Energy (keV)	N/A	N/A	Bremss: N/A G1: 0.423 <sup>+0.010</sup> <sub>-0.011</sub> G2: 0.557 <sup>+0.005</sup> <sub>-0.008</sub> G3: 0.907 <sup>+0.009</sup> <sub>-0.007</sub>
Line Sigma (keV)	N/A	N/A	Bremss: N/A G1: 0.005 <sup>+0.010</sup> <sub>-0.004</sub> G2: 0.028 <sup>+0.008</sup> <sub>-0.010</sub> G3: 0.003 <sup>+0.015</sup> <sub>-0.002</sub>
Flux <sup>d</sup>	16.1 <sup>+118.3</sup> <sub>-15.0</sub>	3.9 <sup>+9.1</sup> <sub>-2.2</sub>	Bremss: 0.32 <sup>+54.0</sup> <sub>-0.03</sub> G1: 0.32 <sup>+109.0</sup> <sub>-0.28</sub> G2: 0.38 <sup>+18.32</sup> <sub>-0.29</sub> G3: 0.032 <sup>+10.9</sup> <sub>-0.015</sub>
$\chi^2_\nu$	1.3 (84)	1.5 (85)	1.3 (87)

§<sup>1</sup>§<sup>2</sup>§<sup>3</sup>The spectral models are fitted simultaneously with the models labeled by the same number in Table 2.

<sup>a</sup>1 keV  $\simeq 1.2 \times 10^7$  K.

<sup>b</sup>Calculated using the normalization constant of the VMEKAL/VPSHOCK thermal plasma models (see sec[4.1]).  $A = (10^{-14}/4\pi D^2) \times EM$  where EM (Emission Measure) =  $\int n_e n_H dV$  (integration is over the emitting volume V).

<sup>c</sup>Calculated using the normalization constant of the Thermal Bremsstrahlung model.

$A = (3.02 \times 10^{-15}/4\pi D^2) \times E.M.$  where E.M. (Emission Measure) =  $\int n_e n_I dV$  (integration is over the emitting volume V).

<sup>d</sup>Unabsorbed Hard X-ray flux between 0.3 and 10 keV in units of  $\times 10^{-12}$  erg cm<sup>-2</sup> s<sup>-1</sup>. The unconstrained parameters are kept at their best fit values when calculating model fluxes.

Table 2: Spectral Parameters of The Entire Spectrum of the Nova Shell for the **Harder X-ray Component** above 2 keV (ranges correspond to  $2\sigma$  confidence level errors)

Model	$N_H$ ( $\times 10^{22}$ cm $^{-2}$ )	$kT_s$ <sup>a</sup> (keV)	$\tau$ ( $\times 10^{11}$ s cm $^{-3}$ )	E.M. <sup>b c</sup> ( $\times 10^{55}$ cm $^{-3}$ )	Flux <sup>d</sup>	$\chi_\nu^2$ <sup>e</sup>
NEI <sup>§1</sup>	14.2 $^{+5.8}_{-11.2}$	0.9 $^{+0.9}_{-0.3}$	0.09 $^{+0.41}_{-0.089}$	3.02 $^{+13.0}_{-2.5}$	27.2 $^{+322.8}_{-25.8}$	...
PSHOCK <sup>§2</sup>	13.7 $^{+7.3}_{-9.7}$	0.96 $^{+1.04}_{-0.4}$	0.0-0.13 $^{+0.27}_{<}$ f	2.2 $^{+11.1}_{-1.9}$	150.0 $^{+50.0}_{-149.6}$	...
BREMSS <sup>§3</sup>	12.9 $^{+9.1}_{-6.9}$	1.04 $^{+1.66}_{-0.5}$	N/A	2.4 $^{+6.4}_{-2.34}$	5.2 $^{+29.8}_{-4.45}$	...
NEI <sup>§1</sup>	0.2 $^{+0.1}_{-0.1}$ g	60.0 $^{<}_{-51.0}$	6.7 $^{<}_{-4.3}$	0.001 $^{+0.001}_{-0.0005}$	0.08 $^{+0.06}_{-0.03}$	2.4
Model	$N_H$ ( $\times 10^{22}$ cm $^{-2}$ )	$\Gamma$	$\alpha$	Break Frequency ( $\times 10^{18}$ Hz)	Flux <sup>d</sup>	$\chi_\nu^2$
POWER <sup>§3</sup>	16.9 $^{+8.1}_{-5.9}$	5.9 $^{+1.2}_{-2.1}$	N/A	N/A	14000.0 $^{+286000.0}_{-13000.8}$	...
SRCUT <sup>§3†</sup>	10.5 $^{+5.5}_{-4.5}$	N/A	0.32 $^{+0.25}_{<}$	0.05 $^{+0.8}_{-0.03}$	6.2 $^{+32.0}_{-5.44}$	...
POWER <sup>§1</sup>	0.29 $^{+0.04}_{-0.04}$ g	0.04 $^{+0.6}_{-0.9}$	N/A	N/A	0.3 $^{+4.0}_{-0.27}$	1.94

<sup>§1§2§3</sup>The spectral models are fitted simultaneously with the models labeled by the same number in Table 1. † The normalization of the SRCUT model (the radio flux at 1 GHz) is frozen at 0.024 Jy at the measured value (Reynolds & Chevalier 1984; Biermann et al. 1995)

<sup>a</sup>1 keV  $\simeq 1.2 \times 10^7 K$ .

<sup>b</sup>Calculated using the normalization constant of the VMEKAL/PSHOCK model.  $A = (10^{-14}/4\pi D^2) \times \text{E.M.}$  where E.M. (Emission Measure) =  $\int n_e n_H dV$  (integration is over the emitting volume V).

<sup>c</sup>Calculated using the normalization constant of the Thermal Bremsstrahlung model.

$A = (3.02 \times 10^{-15}/4\pi D^2) \times \text{E.M.}$  where E.M. (Emission Measure) =  $\int n_e n_I dV$  (integration is over the emitting volume V).

<sup>d</sup>Unabsorbed Hard X-ray flux between 0.3 and 10 keV in units of  $\times 10^{-12}$  erg cm $^{-2}$  s $^{-1}$ .

<sup>e</sup>The values for  $\chi_\nu^2$  are the same as in Table 1 since the two emission models are fitted simultaneously. Thus, they will be omitted from this table.

<sup>f</sup>The range is derived using the values for the two parameters  $\tau_{up}$  and  $\tau_{low}$ .  $\tau_{low}$  is fixed at the value of 0.0 for convenience, since it is the lower limit for the integration over the ionized volume and  $\tau_{up}$  shows the maximum limit on the ionization parameter at  $2\sigma$  confidence level.

<sup>g</sup>This value of  $N_H$  is derived from the fits with a single absorption parameter used for both X-ray spectral components.

Table 3: Spectral Parameters of The Brightest Emission Region of the Nova Shell (ranges correspond to  $2\sigma$  confidence level errors)

Model for Component1	$N_H$ ( $\times 10^{22}$ cm $^{-2}$ )	$kT_s^a$ (keV)	$\tau$ ( $\times 10^{11}$ s cm $^{-3}$ )	Ne/Ne $_{\odot}$	N/N $_{\odot}$	E.M. $^b$ ( $\times 10^{53}$ cm $^{-3}$ )	Flux $^c$	$\chi^2_{\nu}$
VPSHOCK $^{\S 1}$	$0.37^{+0.05}_{-0.04}$ d	$0.1^{+0.04}_{<}$	$0.0-2.8^{<}_{-2.4}$ e	$7.6^{+13.0}_{-6.6}$	$1.9^{+2.2}_{-0.9}$	$0.7^{+0.4}_{-0.2}$	$0.2^{+0.7}_{-0.15}$	... $^f$
VMEKAL $^{\S 2}$	$0.25^{+0.08}_{-0.05}$ d	$0.1^{+0.02}_{-0.01}$	N/A	$7.3^{+7.7}_{-4.1}$	$2.8^{+5.2}_{-1.8}$	$11.7^{+15.0}_{-7.2}$	$2.9^{+12.7}_{-2.2}$	... $^f$
Model for Component2	$N_H$ ( $\times 10^{22}$ cm $^{-2}$ )	$\Gamma$	$\alpha$	Radio Flux at 1 GHz (Jy)	Break Frq. ( $\times 10^{18}$ Hz)	Flux $^c$	$\chi^2_{\nu}$	
POWER $^{\S 2}$	$4.9^{+5.1}_{-3.7}$ d	$2.3^{+1.5}_{-0.9}$	N/A	N/A	N/A	$1.7^{+73.0}_{-1.4}$	1.15	
SRCUT $^{\S 1}$	$5.0^{+3.5}_{-1.7}$ d	N/A	$0.68^{+0.03}_{-0.15}$	0.024	$1.2^{+2.3}_{-0.3}$	$1.7^{+125.3}_{-1.6}$	1.16	
POWER $^{\S 2}$	$0.38^{+0.17}_{-0.23}$ g	$-0.2^{+0.7}_{-0.8}$	N/A	N/A	N/A	$30.0^{+55.0}_{-18.0}$	1.9	
SRCUT $^{\S 1}$	$0.40^{+0.06}_{-0.15}$ g	N/A	$0.87^{+0.06}_{-0.02}$	0.024	$4.5^{<}$	$0.03^{+0.02}_{-0.01}$	3.0	
Model for Component2	$N_H$ ( $\times 10^{22}$ cm $^{-2}$ )	$kT_s^a$ (keV)	$\tau$ ( $\times 10^{11}$ s cm $^{-3}$ )	E.M. $^b$ ( $\times 10^{53}$ cm $^{-3}$ )	Flux $^c$	$\chi^2_{\nu}$		
PSHOCK $^{\S 2}$	$4.2^{+5.0}_{-1.8}$ d	$20.9^{<}_{-17.0}$	$96^{<}_{-95.9}$	$1.1^{+14.6}_{-0.5}$	$0.8^{+10.7}_{-0.4}$ <	1.7		
MEKAL $^{\S 1}$	$0.38^{+0.17}_{-0.16}$ g	$20.0^{<}_{-13.0}$	N/A	$0.3^{+0.2}_{-0.2}$	$0.2^{+1.13}_{-0.13}$	2.8		

$^{\S 1\S 2}$ The spectral models are fitted simultaneously with the models labeled by the same number.

$^a$ 1 keV  $\simeq 1.2 \times 10^7 K$ .

$^b$ Calculated using the normalization constant of the (V)MEKAL/(V)PSHOCK models.  $A = (10^{-14}/4\pi D^2) \times \text{E.M.}$  where E.M. (Emission Measure) =  $\int n_e n_H dV$  (integration is over the emitting volume V).

$^c$ Unabsorbed Hard X-ray flux between 0.3 and 10 keV in units of  $\times 10^{-13}$  erg cm $^{-2}$  s $^{-1}$ . The unconstrained parameters are kept at their best fit values when calculating model fluxes.

$^d$ This value of  $N_H$  is derived from the fits with two different absorption parameter used for the two X-ray spectral components.

$^e$ The range is derived using the values for the two parameters  $\tau_{up}$  and  $\tau_{low}$ .  $\tau_{low}$  is fixed at the value of 0.0 for convenience, since it is the lower limit for the integration over the ionized volume and  $\tau_{up}$  shows the maximum limit on the ionization parameter at  $2\sigma$  confidence level.

$^f$ The values for  $\chi^2_{\nu}$  are listed with the parameter results for Component 2 since the two emission models are fitted simultaneously.

$^g$ This value of  $N_H$  is derived from the fits with a single absorption parameter used for both X-ray spectral components.

Fig. 1.— The X-ray nebula around the classical nova Persei (1901) between 0.3 and 10 keV obtained with the *Chandra* ACIS-S (S3). The image shows emission  $2\sigma$  above the background. The resolution is  $0''.5$  per pixel. It is smoothed using a variable Gaussian filter with  $\sigma=0''.5-1''$ . North is up and West is to the right. Central source is extracted from the image using a modeled PSF (see section 4.1) created with the aid of ChaRT, and MARX.

Fig. 2.— The X-ray data of the shell fitted with the VMEKAL+PSHOCK emission models including two different neutral hydrogen absorption. The smooth curve is the *Chandra* ACIS-S response to the composite model spectrum and the actual ACIS-S data are indicated with crosses. The dashed line shows the contribution of the VMEKAL model whereas the dot-dashed line indicates the contribution from the PSHOCK model of emission. The lower panel shows the residuals between the data and the model in standard deviations. In general, solar elemental abundances are assumed except for neon and nitrogen.

Fig. 3.— (a) The source count rates extracted from an aperture of  $12''.5$  versus the source count rates detected within an annular region from  $12''.5$  to  $67''.5$  in radius. It shows a scaling relation between the source count rates (largely piled-up) and the count rates derived from the PSF wings in the  $2'$  vicinity of the pointed source. Both count rates are background subtracted. (b) The example calibration point source spectra used in Figure 3a. The central source count rate (pileup rate) increases from  $0.19$  to  $0.21$   $\text{c s}^{-1}$  from row 1 column 1 to row 2 col 2. The upper curves are the spectra from the *source*-region and the lower curves are spectra from the *shell*-region as denoted in the text.

Fig. 4.— The top crosses (curve) indicate the data of the central source spectrum derived from an aperture of  $12''.5$  (includes pileup photons). The middle crosses (curve) show the simulated central source spectrum scaled to match the expected count rate from the location covered by the X-ray shell which is  $0.037$   $\text{c s}^{-1}$ . The middle curve is the expected spectrum of the PSF wings for GK Per. The lower crosses (curve) is the un-piled central source spectrum (of GK Per) derived from the out-of-time events of the ACIS transfer streak.

Fig. 5.— (a) The X-ray data of the shell cleaned from the effects of the PSF wings of the central source and fitted with a single model of emission (VPSHOCK) together with a neutral hydrogen absorption model. The figure stresses the significant deviation above 1.6 keV. (b) The X-ray data of the shell cleaned from the effects of the PSF wings of the central source and fitted with the VPSHOCK+NEI emission models including two different neutral hydrogen absorption models. The smooth curve is the *Chandra* ACIS-S response to the composite model spectrum and the actual ACIS-S data are indicated with crosses. The dashed line shows the contribution of the VPSHOCK model whereas the dot-dashed line indicates the contribution from the NEI model of emission. The lower panel shows the

residuals between the data and the model in standard deviations. (c) The same plot as in (b), but has only a single neutral hydrogen absorption parameter for both of the components. This spectrum is regrouped to have a Signal-to-Noise ratio of 13 per energy bin.

Fig. 6.— (a) The figure shows several extraction regions used to derive the spectra to study the spectral variation within the remnant. The large circle is divided into 4 quadrants of SW, NW, NE, SE. The other three regions are constructed to study the brightest X-ray region. The extraction region is a PIE (annulus-sector as noted in the text) with (1) denoting the inner ridge, (2) the Peak X-ray zone, and (3) the outer ridge. (b) The X-ray data fitted with the VMEKAL+PSHOCK emission models including neutral hydrogen absorption. The figure shows four spectra obtained by dividing the shell into four quadrants centered on the NE, SE, NW and SW with an inner radius of  $12''.5$  and an outer radius of  $67''.5$ .

Fig. 7.— (a) The X-ray data fitted with a single model of emission (VPSHOCK) together with a single neutral hydrogen absorption model. This figure stresses the significant deviation of the residuals above 1.6 keV and the existence of the second component. (b) The X-ray data fitted with the VPSHOCK+SRCUT emission models including two different neutral hydrogen absorption. The smooth curve is the *Chandra* ACIS-S response to the composite model spectrum and the actual ACIS-S data are indicated with crosses. The dashed line shows the contribution of the VPSHOCK model whereas the dot-dashed line indicates the contribution from the SRCUT model of emission. The lower panel shows the residuals between the data and the model in standard deviations. (c) The same plot as in (b), but has only a single neutral hydrogen absorption parameter for both of the components.

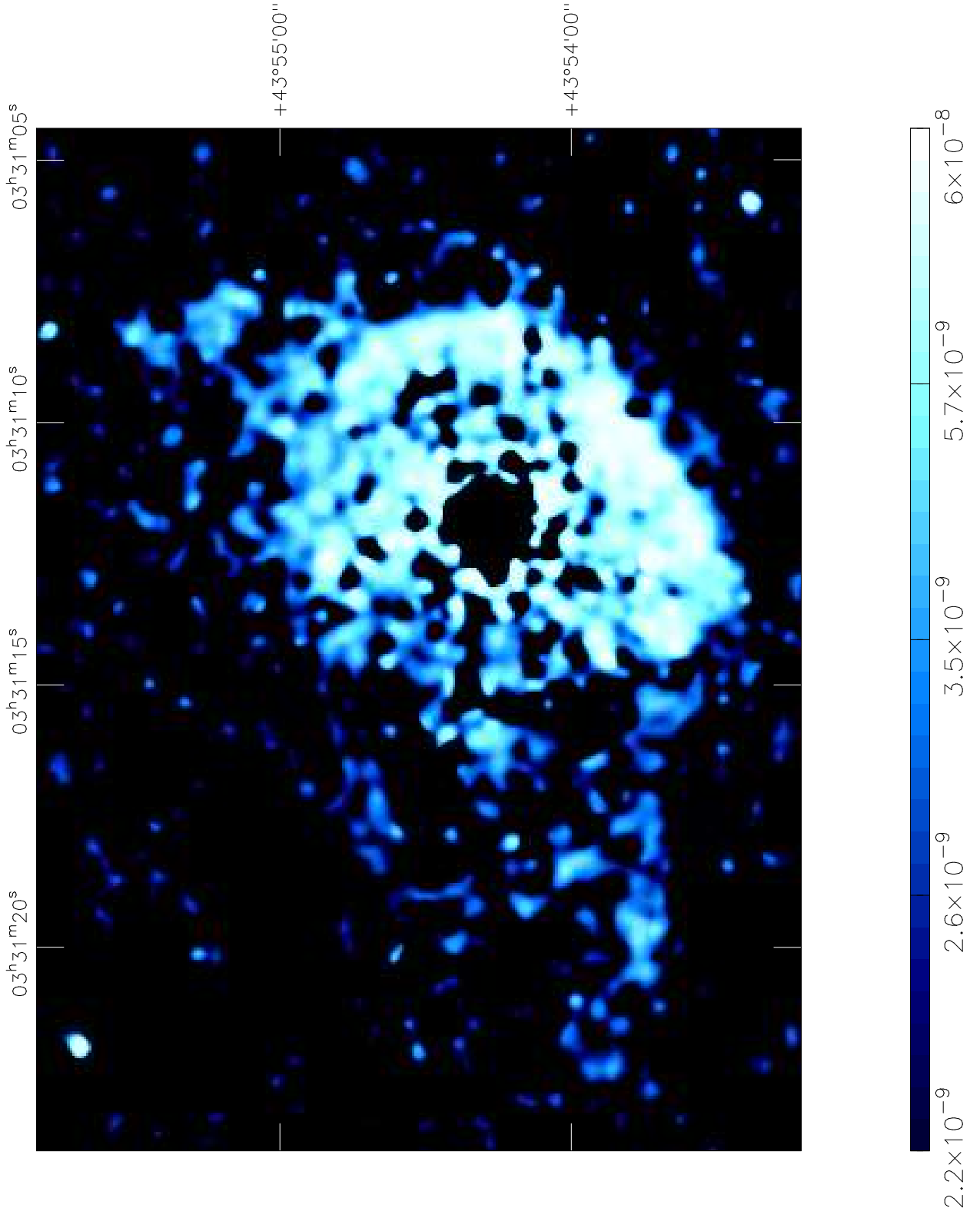
Fig. 8.— The image of the X-ray nebula extracted from 0.8 to 1.0 keV around the He-like Ne IX emission line. A suitable continuum between energy channels 1.12-1.4 (corresponding to the amount of energy channels within the line at the continuum level) is subtracted from the image. The resolution of the image is  $1''$  per pixel. North is up and West is to the right. The image is smoothed using a Gaussian filter with  $\sigma=2''$ . The cross point shows the location of the central source.

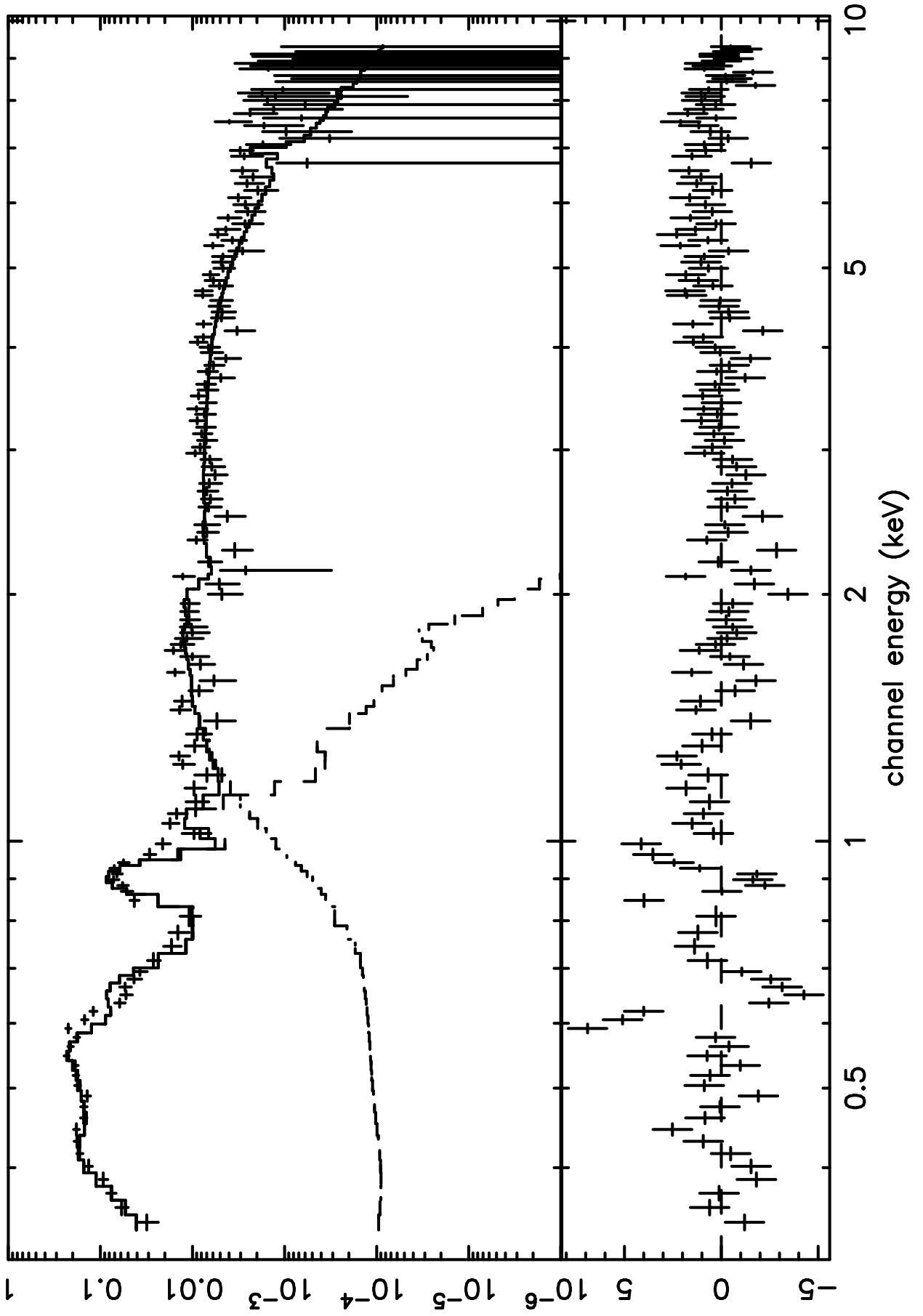
Fig. 9.— (a) The left-hand panel is the image of the X-ray nebula in the 0.25-0.50 keV energy band, (b) The middle panel is the image of the X-ray nebula in the 0.51-1.50 keV energy band. The two images in (a) & (b) show two sigma emission above the background at  $1''/\text{pixel}$  resolution, smoothed using a Gaussian filter with a variable  $\sigma=1''\text{-}2''$ . (c) The right-hand panel is the image of the X-ray nebula in the 1.51-8.0 keV energy band at a lower resolution of  $3''/\text{pixel}$  (compared with (a) & (b)) smoothed using a Gaussian filter with a  $\sigma=6''$ . The image in (c) shows three sigma emission above the background. The overlay are contours of the 0.51-1.50 keV image produced at the same spatial resolution and smoothed

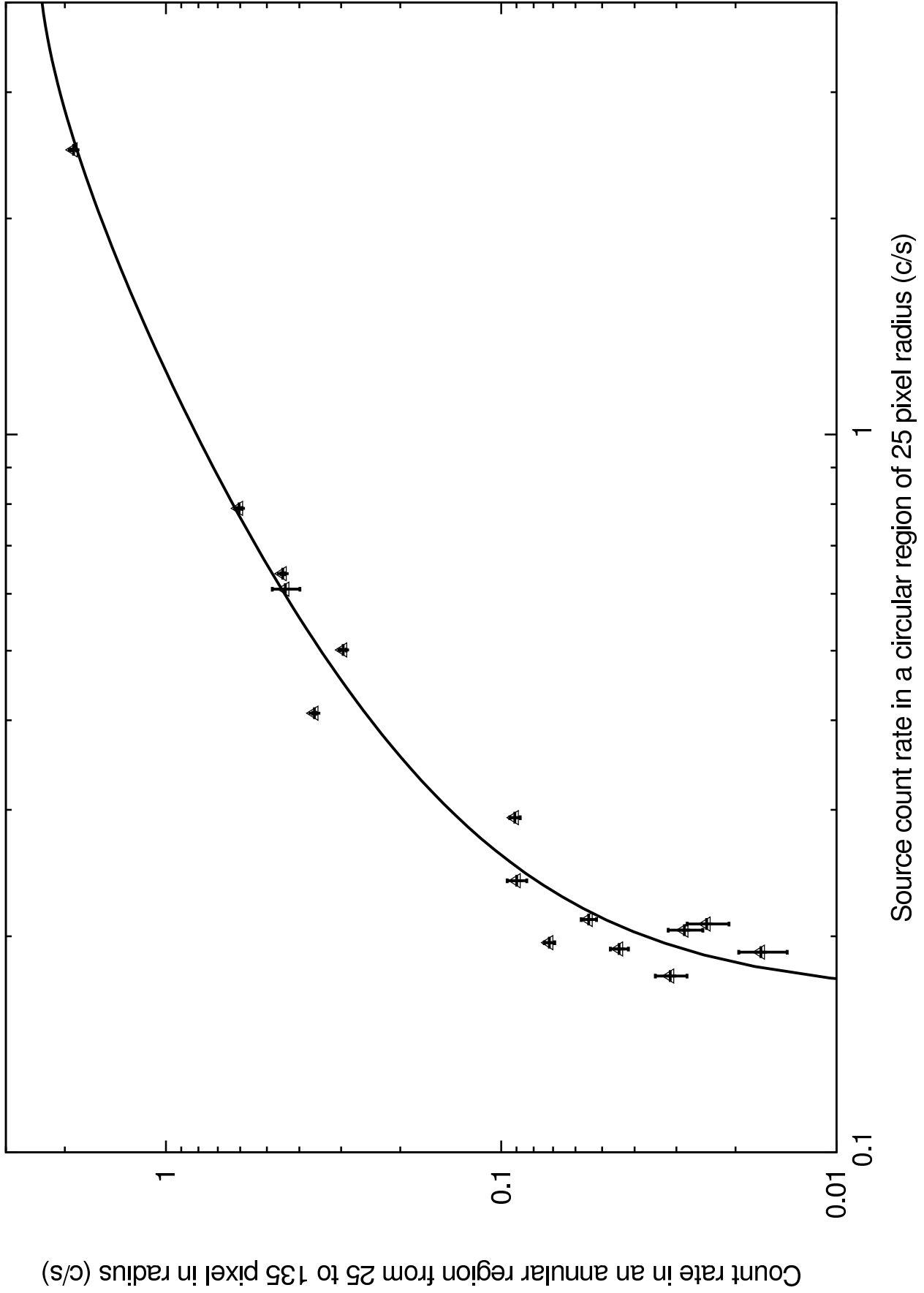
using the same Gaussian.

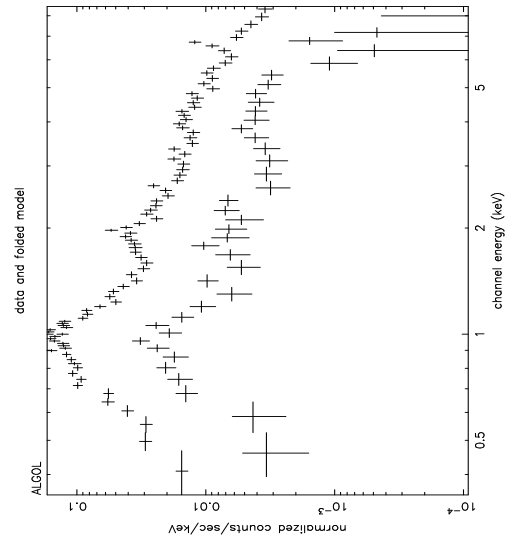
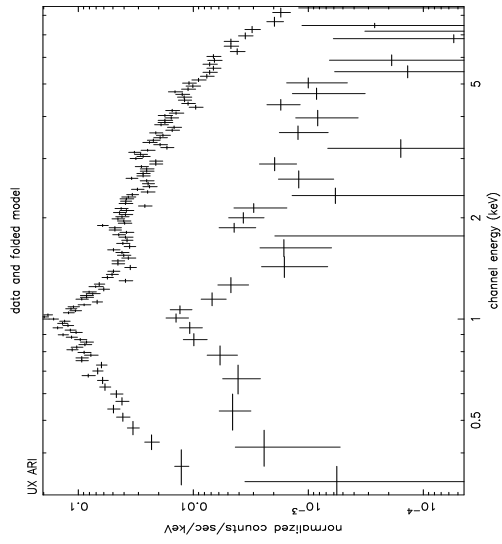
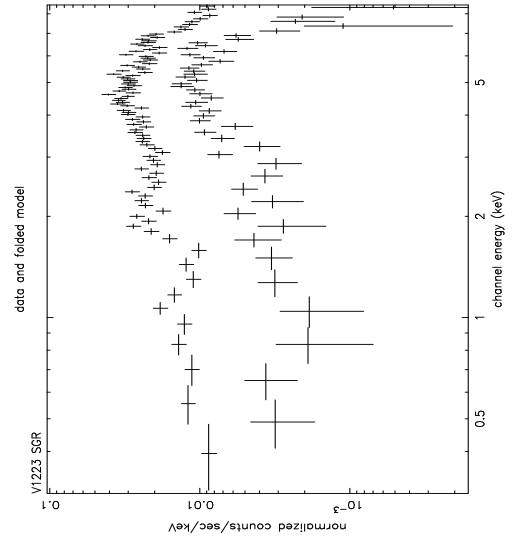
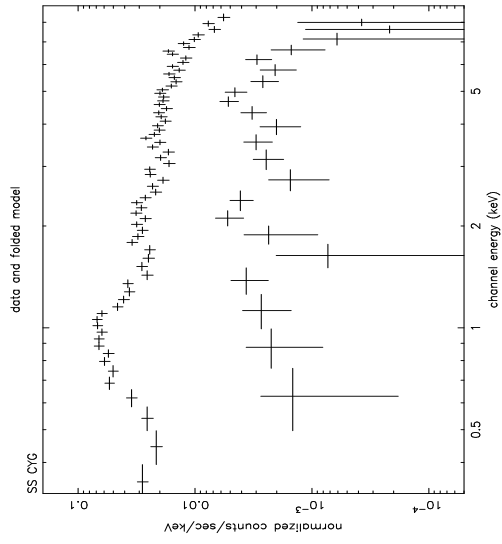
Fig. 10.— (a) The figure shows the intensity contours of the HST image (1997) obtained with the [NII] filter overlaid on the X-ray image of shell of GK Per. Both the HST contours and the X-ray image show emission  $2\sigma$  above the background. The resolution of the combined image is  $2''$  per pixel. Both images are also smoothed by a Gaussian filter with  $\sigma=2''$ . The [NII] intensity contours are based on histogram equalization starting with  $0.6\sigma$  to  $68\sigma$  increments between contour levels. (b) The figure shows the radio intensity contours at 1.425 GHz overlaid on the X-ray image of the shell of nova Persei (1901). The X-ray image and the radio contours show emission  $2\sigma$  and  $1.5\sigma$  above the background, respectively. The resolution of the combined image is  $2''$  per pixel. Both images are also smoothed by a Gaussian filter with  $\sigma=1''$ . The radio intensity contours are constructed with linear  $1.4\sigma$  increments between contour levels.

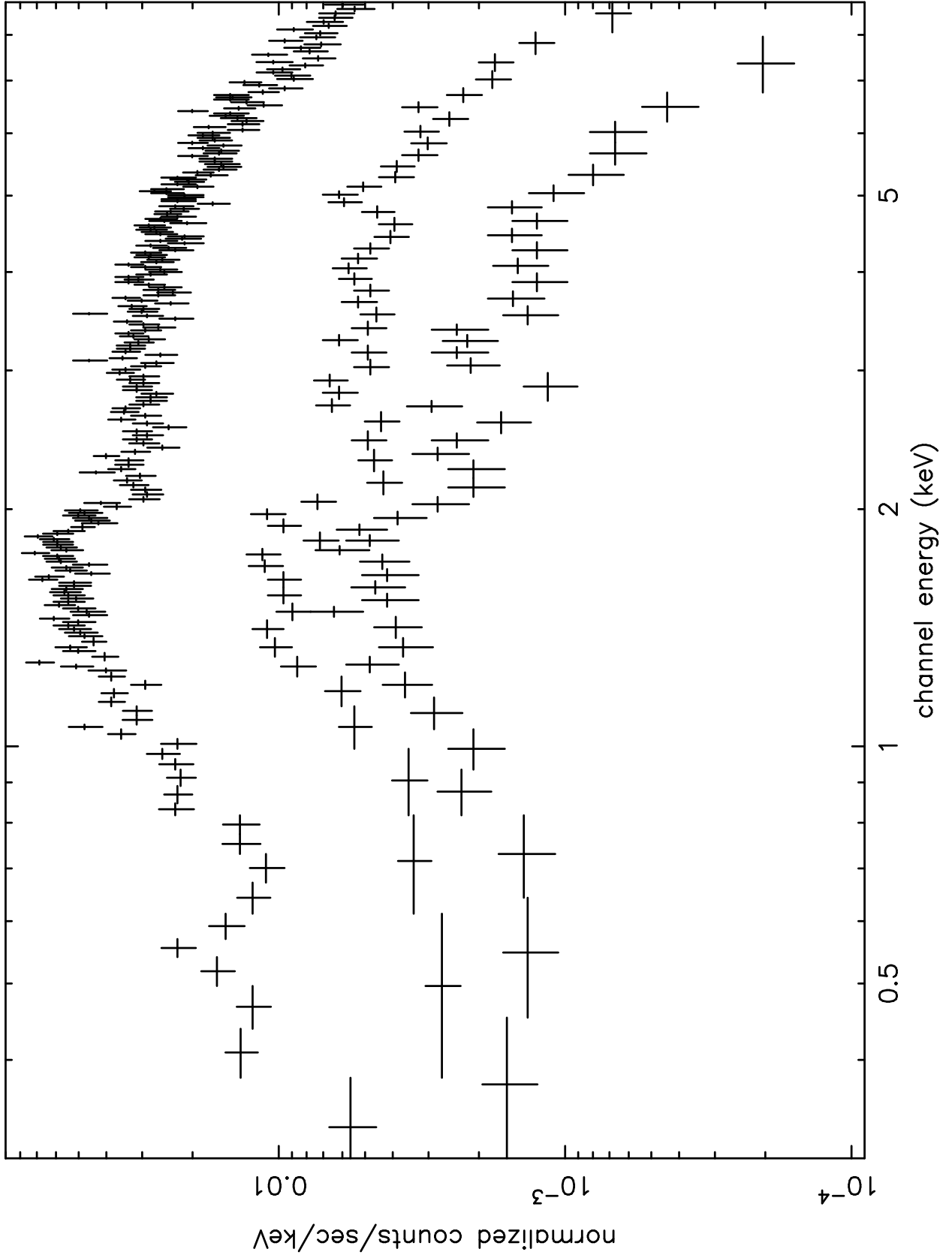


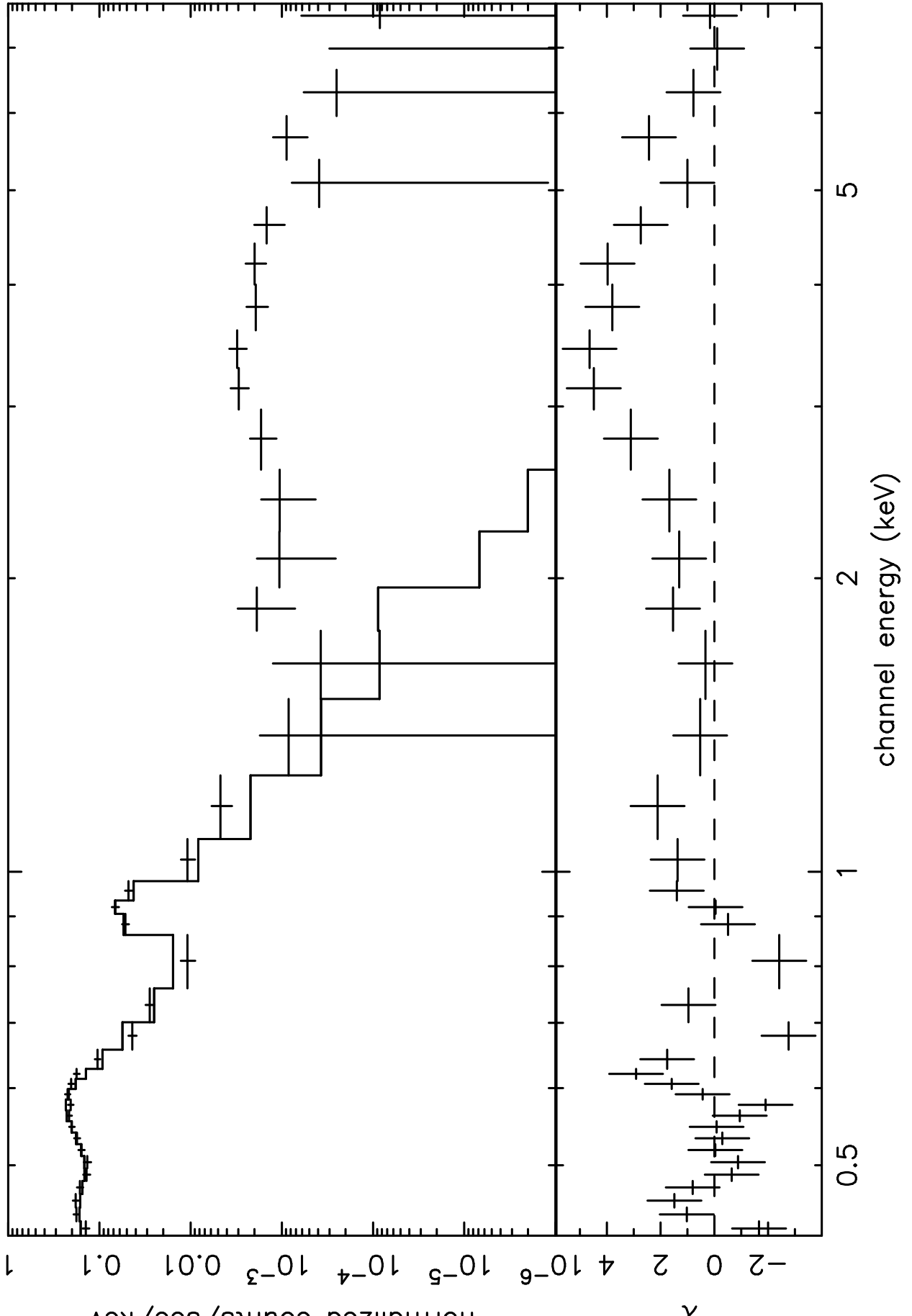


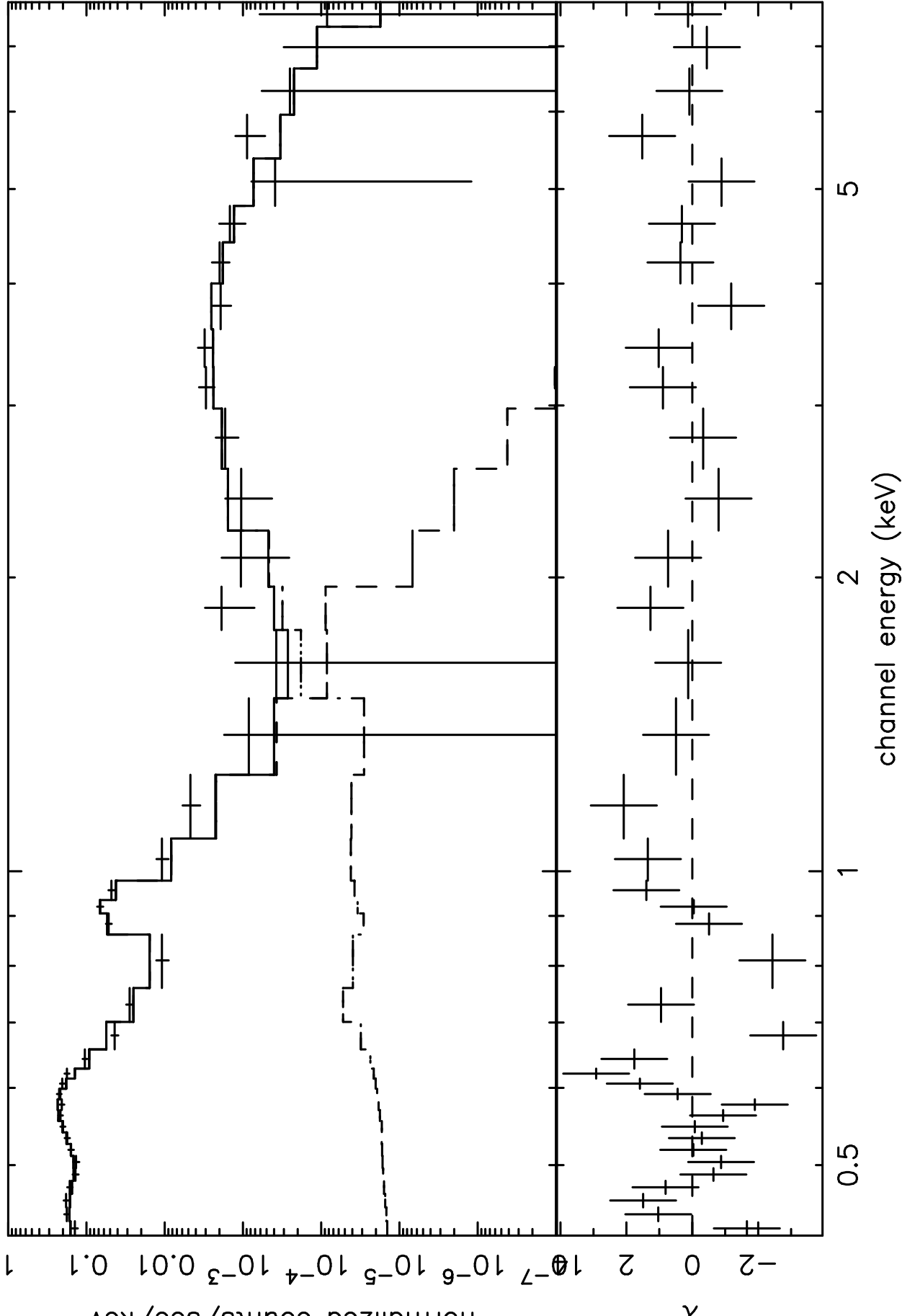


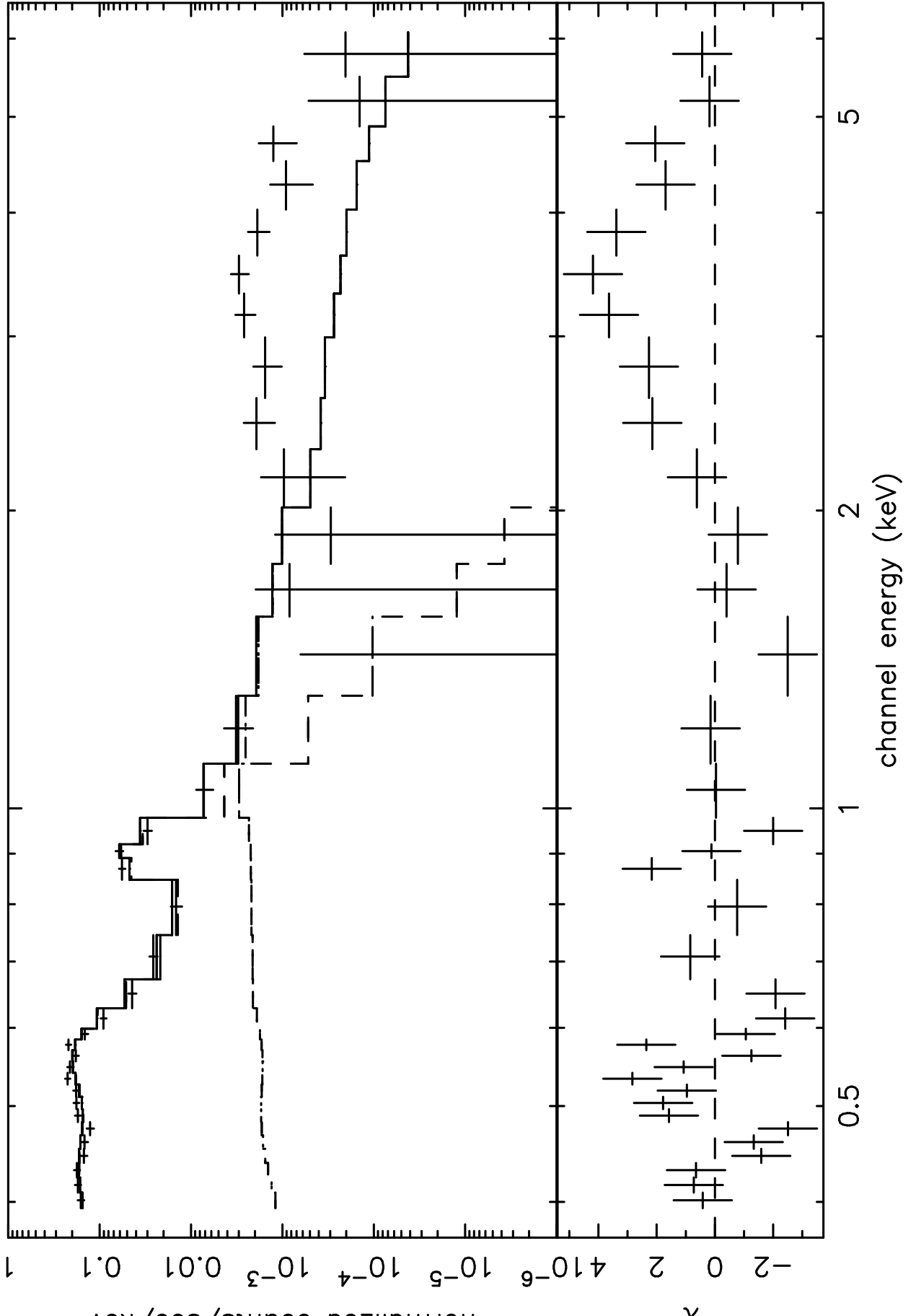




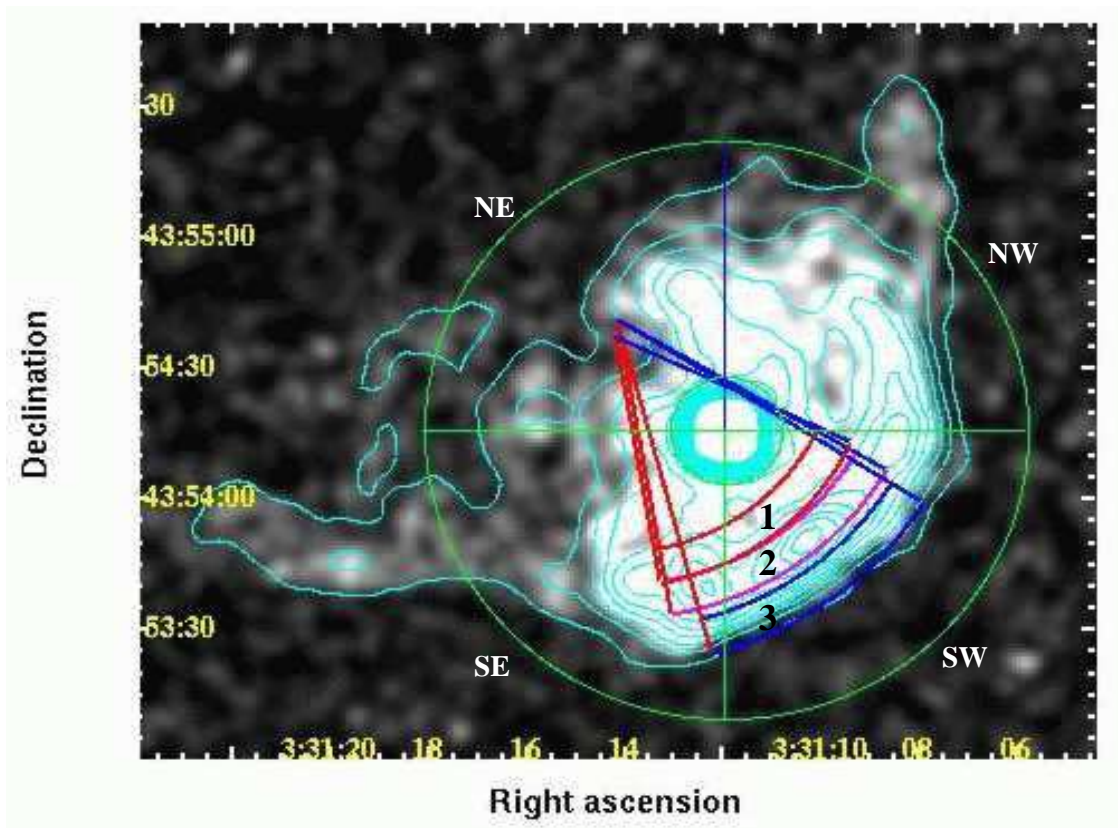


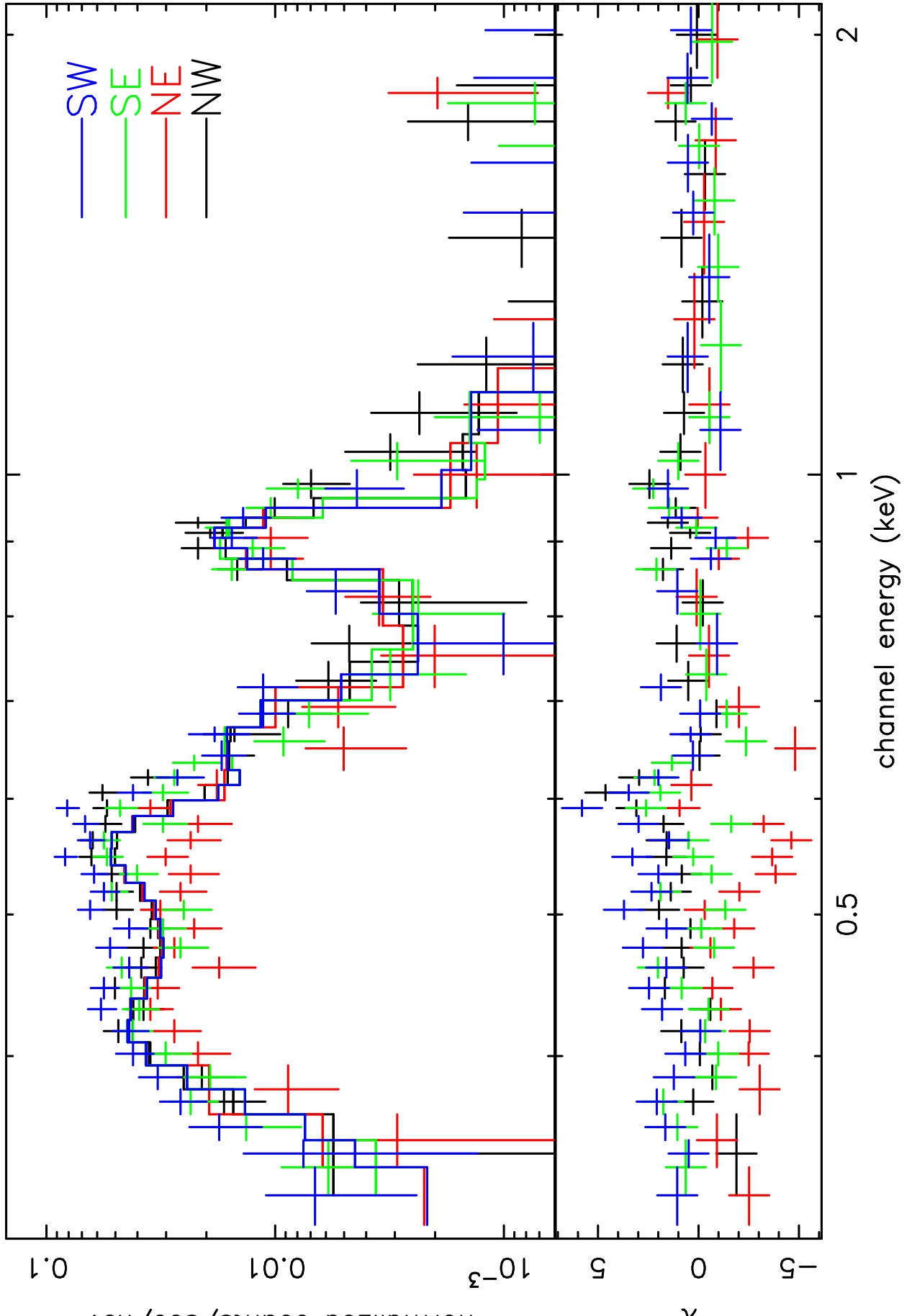


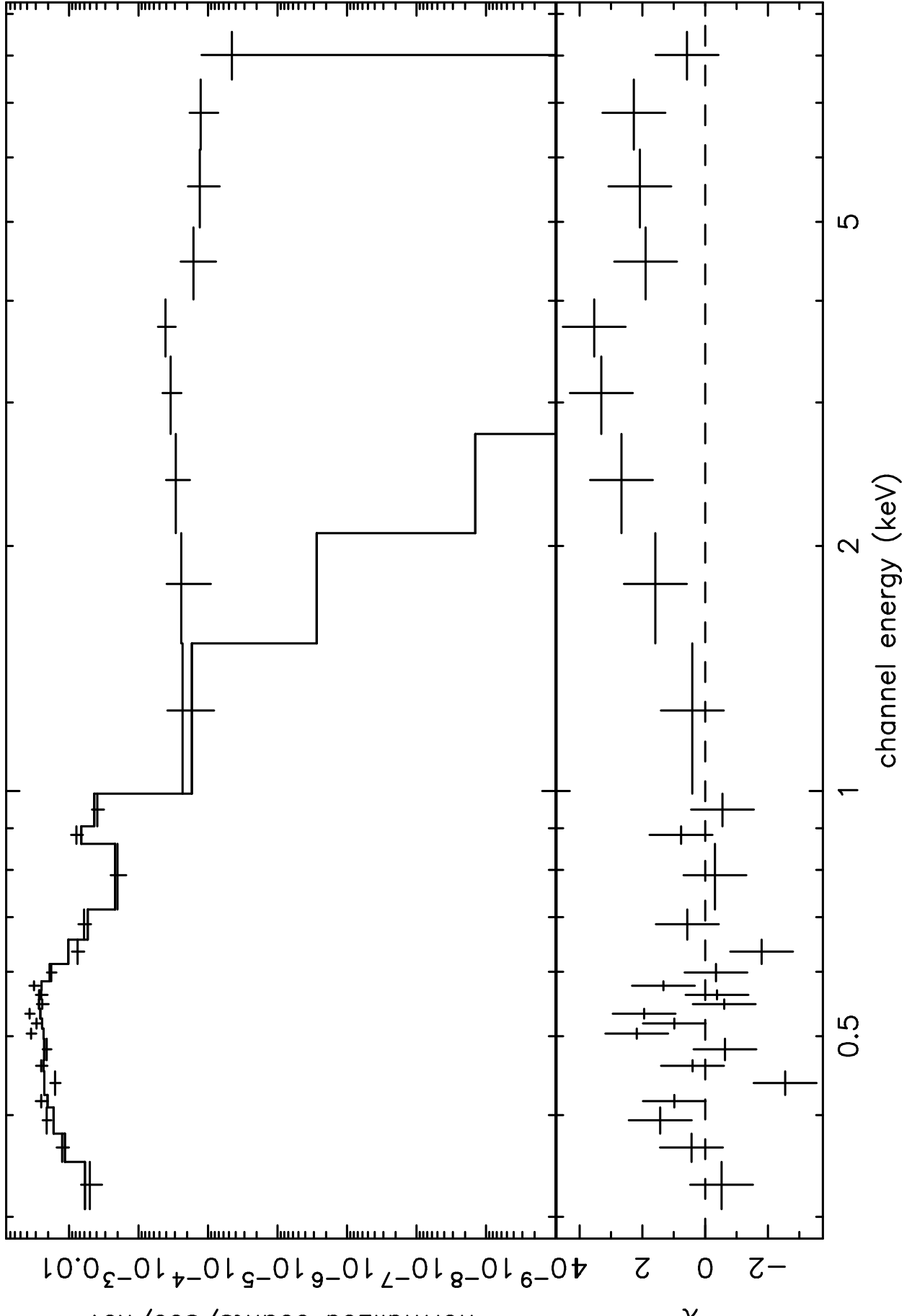


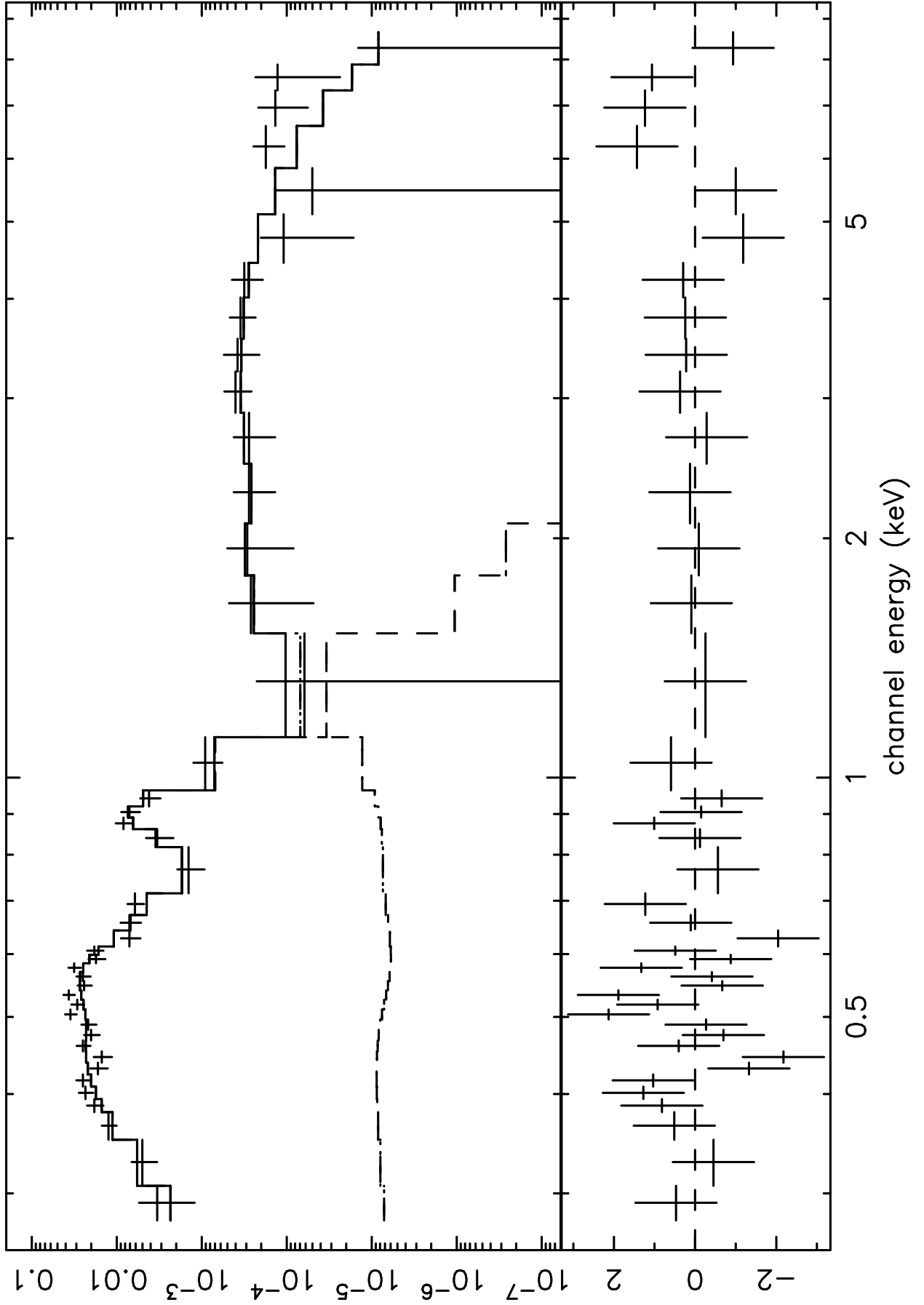


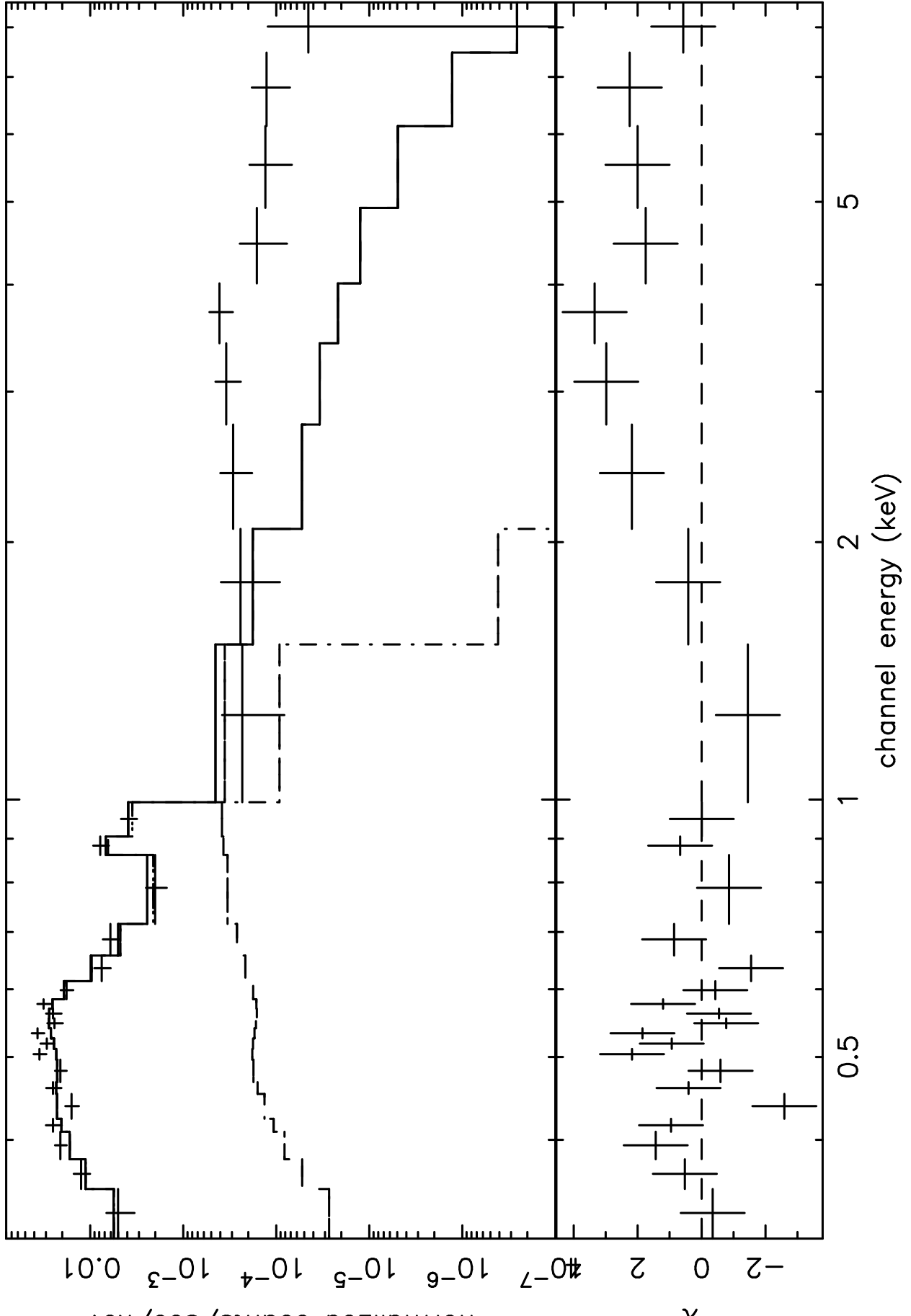


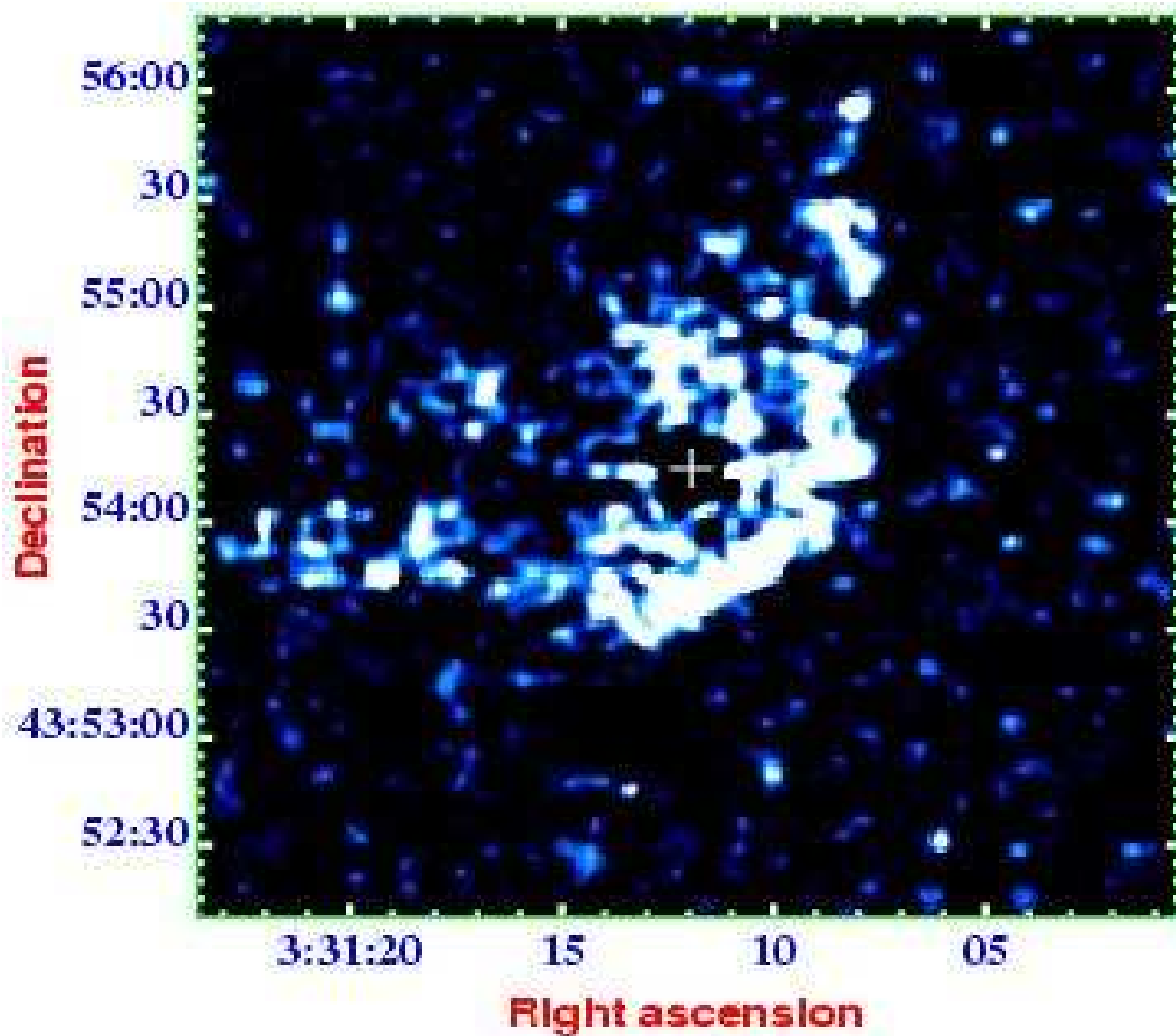








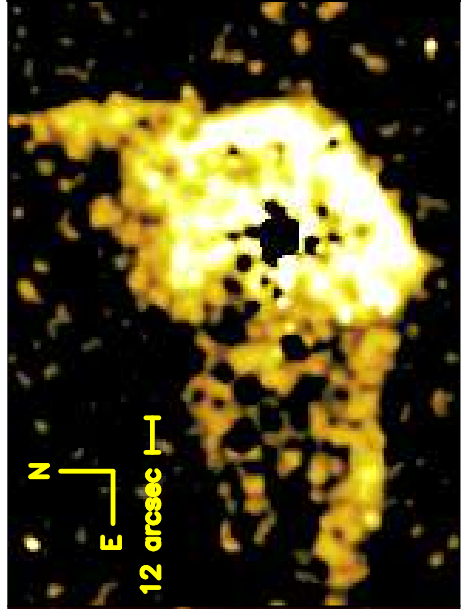




(0.25–0.5 keV)



(0.51–1.5 keV)



(1.51–8.0 keV)



